Topics in Current Chemistry (2020) 378:2
https://doi.org/10.1007/s41061-019-0262-3

REVIEW

# Mechanochemical Forces as a Synthetic Tool for Zero- and One-Dimensional Titanium Oxide-Based Nano-photocatalysts

**Dimitrios A. Giannakoudakis[1] · Gregory Chatel[2] · Juan Carlos Colmenares[1]**

Received: 30 July 2019 / Accepted: 22 October 2019 / Published online: 25 November 2019


## Abstract

A new field where the utilization of mechanochemistry can create new opportunities is materials chemistry, and, more interestingly, the synthesis of novel nanomaterials. Ball-milling procedures and ultrasonic techniques can be regarded as the most important mechanochemical synthetic tools, since they can act as attractive alternatives to the conventional methods. It is also feasible for the utilization of mechanochemical forces to act synergistically with the conventional synthesis (as a pre-treatment step, or simultaneously during the synthesis) in order to improve the synthetic process and/or the material's desired features. The usage of ultrasound irradiation or ball-milling treatment is found to play a crucial role in controlling and enhancing the structural, morphological, optical, and surface chemistry features that are important for heterogeneous photocatalytic practices. The focus of this article is to collect all the available examples in which the utilization of sonochemistry or ball milling had unique effects as a synthesis tool towards zero- or one-dimensional nanostructures of a semiconductor which is assumed as a benchmark in photocatalysis, titanium dioxide.

This article is part of the Topical Collection "Heterogeneous Photocatalysis"; edited by Mario J. Muñoz-Batista, Alexander Navarrete Muñoz and Rafael Luque.

✉ Dimitrios A. Giannakoudakis
dagchem@gmail.com

✉ Juan Carlos Colmenares
jcarloscolmenares@ichf.edu.pl

[1] Institute of Physical Chemistry, Polish Academy of Sciences, Kasprzaka 44/52, 01-224 Warsaw, Poland

[2] Université Savoie Mont Blanc, LCME, 73000 Chambéry, France

**Graphical Abstract**

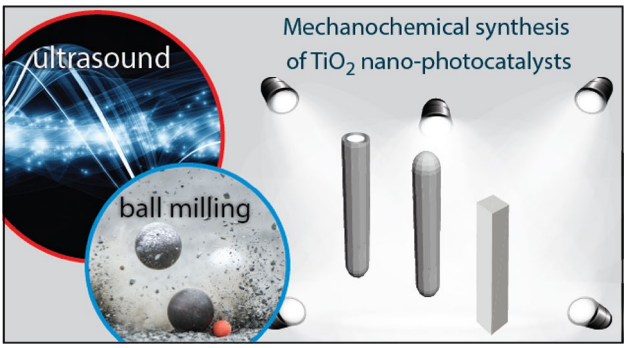


**Keywords** Mechanochemistry · Sonochemistry · Ultrasound-assisted synthesis · One-dimensional titanium oxide · Photocatalysis · Ball milling

## 1 Introduction

### 1.1 Nanotechnology and Photocatalysis

Generally, the impact of nanotechnology has been astonishingly positive in the last decades toward a wide range of environmental, energy, catalysis, as well as synthetic applications and technologies, with a continuous incremental trend of published peer-reviewed articles. Nanostructured and nanoengineered materials garner continuously enhanced research attention and focus due to their unique and novel properties, especially in comparison to bulk materials/counterparts. Application of nanoscaled materials covers a broad range of fields, from electronics and catalytic reactions, to medical and environmental remediation, while novel nanomaterials for new applications are highly desired. The properties of nanomaterials depend on the morphological (shape and size), structural (surface area and porosity), optical (band-gap and light-harvesting capability), and surface chemistry features (nature and availability of the reactive sites). Another important aspect is to obtain well-defined phase composition of high homogeneity. All the above features are directly linked and dependent on the method/protocol of preparation [1]. By tuning specific synthetic parameters, such as temperature, aging, and washing protocol, it is feasible to control the vital features for a targeted use. For instance, the chemical composition and the porosity are crucial features regarding catalytic synthesis and environmental applications. On the other hand, the optical and morphological features are more important for fabricating crystals for photonic devices.

Another important target in laboratory as well as in industrial research is to find novel ways to conduct reactions following "green" approaches. And toward this direction, photocatalysis is a favorable tool, since it is feasible to utilize a natural source of energy, solar light. The harvesting of light from a photocatalyst can

promote specific reactions even without the use of additive chemicals or another source of energy. The most important part in heterogeneous photocatalysis is the development and usage of materials that can function as sufficient photocatalysts, and nanotechnology has been shown capable of providing solutions. Synthesis of nanomaterials and tuning specific features of them like nano-morphological and optical features is an ultimately important and efficient strategy to achieve the above. Even though the synthesis of nanoscaled photocatalysts has been a hot topic during the last decades with many published articles and end-use applications, the use of mechanochemical-based synthetic approaches is not so broadly explored. By gathering the existing knowledge on the effects derived from the mechanochemical forces like ultrasound (US) irradiation and ball milling, it will be realistic to go a step further. The focus of this work is to collect all the reports in which the two above-mentioned techniques were applied during the synthesis of two benchmark semiconductor photocatalysts, titanium dioxide or titanate, in order to obtain various polymorphs with different structural, morphological, and optical features.

### 1.2 Mechanochemical Synthesis

The exploration and discovery of new synthetic approaches as well as the incorporation of advantageous techniques for the development of new or improved properties of already known nanomaterials as photocatalysts is an ongoing and interesting field of research, with fascinating potential [1, 2]. In recent years, mechanochemical processes were found to hold great promise, since they are effective and can lead to nanomaterials of novel properties. Another important aspect is that various reported active nanocatalysts can be synthesized in a shorter time compared to traditional wet-chemistry synthesis. In many cases, the design of mechanochemical-based methods can have a positive effect on the "green" character and environmental footprint: consumption of less energy, less or even no use of hazardous solvents, need of recycling, purification, etc. According to the International Union of Pure and Applied Chemistry (IUPAC), the definition of a mechanochemical process is: "*a chemical reaction that is induced by the direct absorption of mechanical energy*" [3]. The utilization of mechanochemical forces holds great promise and begets novel approaches in nanocrystalline synthesis (mechanosynthesis), and, more specifically, on how to control the desired features, crucial for different applications [3–7]. Herein, two mechanochemical sources will be introduced: (1) US irradiation (sonochemistry) and (2) ball milling. The rapid growth of the research interest around the utilization of mechanochemistry methods is due to their unique effects. By the correct selection of these effects, it is feasible to obtain novel nanomaterials, and to control desired physical, chemical, and optical properties [5, 8]. Simultaneously, it is possible to eliminate the environmental footprint of the synthesis, avoiding, for instance, the usage of high energy, hazardous and non-recyclable chemicals, or by decreasing the duration and the number of steps of the synthesis [9].

## 1.3 Sonochemistry

### 1.3.1 A Brief History

Sound waves not detectable by the human ear with frequencies ranging from 20 kHz to 200 MHz are referred to as ultrasound (US) waves [10]. The effects of sonication are linked to the cavitation phenomena, and they can be chemical, physical, mechanical, or optical. The first reference to the cavitation phenomena by Thornycroft and Barnaby dates from 1895 [11]. By the time Neppiras introduced the term "sonochemistry" in 1980 [12] and Makino et al. showed the formation of radical species during the sonolysis of water in 1982 [13, 14], the research attraction of sonochemistry had increased dramatically. In general, sonochemistry is linked with the understanding and interpretation of the processes and the effects initiated by US irradiation due to the cavitation phenomena. The main derived results are the enhancement of the reaction rate, radical species formation, as well as mass and heat transfer [1, 2, 4, 15–17].

### 1.3.2 Cavitation Phenomena—Mechanistic Aspects on "How Does Everything Work?"

The formation of cavitation bubbles is due to pressure changes upon the travel of US waves in a liquid. The initially formed microbubbles, consisting of vaporized solvent or/and dissolved gases, grow continuously in size by absorbing energy during the irradiation [18]. After growing to a certain size, they violently collapse, creating a localized "hot spot." The local pressure and temperature can be above 1000 bars and 5000 K, respectively [18–20]. The hot-spot concept and the consequential effects can be described by distinguishing three zones [21, 22]. Zone 1 is inside the bubble (primary sonochemistry), zone 2 is at the gas–liquid interface (secondary sonochemistry), and zone 3 is the bulk liquid phase surrounding zone 2. At the interior of the cavity, cleavage of bonds and formation of radicals occurs due to the harsh energetical environment and to the fact that the gaseous concentration is extended [22–24]. These radical species can also be transported to zone 2, where reaction of free radicals and pyrolysis can take place, or even to the bulk liquid zone 3. In an aqueous environment, the sonolysis of water can lead to the formation of hydroxyl ($HO^{\cdot}$) or hydroperoxyl ($HO_2^{\cdot}$) radicals, and hydrogen peroxide ($H_2O_2$). These species can initiate secondary reactions that can play a key role in material synthesis or for catalytic reactions [15].

Even if the "hot-spot" theory is the most accepted to explain these phenomenas, several studies lead to the proposition of plasma [25, 26], electrical [27], and supercritical water [28] theories, demonstrating that all the mechanisms involving US are not completely known. In addition to the chemical effect of US, various other mechanisms exist, such as physical, mechanical, or light emission (sonoluminescence). The latter one is also valuable in order to determine the active regions and intensity of the US waves using a hydroxyl radical trapping agent, luminol (through chemiluminescence [29–31]. The physical/mechanical effects can be the formation of microjets, turbulence, microstreaming, shockwaves, and agitations [23]. These effects can

positively promote the reaction rates by affecting the mass (mixing) and heat transfer phenomena or resulting in some structural alterations of the solids, such as erosion, exfoliation, fragmentation, or deformation [6, 8, 22, 32, 33].

The utilization of US irradiation is a complex aspect, since the formation of cavitation in liquids can be affected by numerous parameters [2, 22, 23]. Some of them are described in most of the articles, but some were not reported. The frequency and the power of the irradiated US waves can be considered the most fundamental parameters [16]. Increase of the US frequency leads to shortening of the expansion and compression pressure cycle, and, as a result, to a negative impact on the effectiveness. The formed bubbles/cavitation at higher frequencies have a smaller size and less violent implosion effects, although they have a better size distribution and rate formation. At lower frequency, the cavitation phenomena is more violent and intense with a consequent of higher localized pressure and temperature, as well as higher concentration of free radical formation. However, there are many cases where the high frequencies have desired impact on reaction rates and material synthesis.

Other important parameters that should be taken into consideration for the effective US utilization in synthesis of catalysts and catalytic reactions are the solvent, the presence/concentration of dissolved gases, temperature, and pressure [34]. The physicochemical parameters of the solvent, for example, the solubility of air or oxygen, viscosity, surface tension, or vapor pressure, play key roles in the cavitation threshold. The increment of the latter parameter has a negative impact on the cycle formation, while, on the contrary, increment of the rest has a positive effect. Initiation of cavitation is facilitated by the presence of dissolved gases. However, the extent of the assistance upon cavitation is related to the physical properties of the gas. Contrary to the chemical processes, the increase of the temperature (until a specific range) has a negative impact on the sonochemical reaction due to increase of the vapor pressure and to the decrement of the gaseous solubility. However, there are many circumstances revealing that the temperature increase has positive and desired effects. An increase of the reactor pressure could cause a decrease of the solvent's vapor pressure.

## 1.4 Ball Milling

### 1.4.1 A Brief History

The earliest recorded mechanochemical process, according to Takacs [35], dates to the fourth century BC, in which Theophastus of Eresos noted the synthesis of elemental mercury by grinding cinnabar (HgS) with acetic acid in a Cu vessel, the first documented separation of an elemental metal [3, 7, 35]. Since a solvent was needed even in a minimal amount, this process is regarded nowadays as liquid-assisted grinding (LAG). From this point and afterward, mechanochemistry-based approaches were applied widely in metallurgy and mining, and more details can be found elsewhere [35–37]. By the use of a pestle and mortar and without a liquid (dry grinding), it was the great experimental physicist, Michael Faraday (discovered the laws of electrolysis, electromagnetic induction, and the rotation of polarized light by

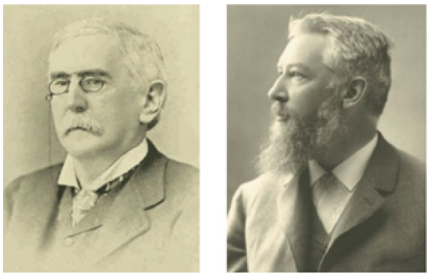

**Fig. 1** Mathew Carey Lea (1823–1897) and Friedrich Wilhelm Ostwald (1853–1932) left and right, respectively. Reprinted with permission from [40]. Copyright (2013) Royal Society of Chemistry

magnetism) who conducted displacement reactions between a metal and oxides of less reactive metals [3, 7, 35]. In his first research published in 1820, which can be assumed as the first systematic study of the mechanochemical process, he showed the oxidation of Zn by the reduction of AgCl to Ag by simple mortar grinding [35, 38]. However, there was no specific evidence indicating if the grinding promoted the reaction mechanochemically of just thermodynamically by heat generation through friction.

The American chemist and pioneer of photographic chemistry, Mathew Carey Lea (1823–1897), systematically studied and determined (between 1889 and 1894) that the above kind of redox reactions were initiated/activated by mechanochemical effects rather than thermochemical effects. A clear and loud example was the formation of elemental Ag from grinding of silver halides, while it was just melted without decomposition upon thermal treatment [39] (Fig. 1).

The terminology of mechanochemistry was introduced by L. Crismer in 1912 in a biography of Walthere Spring and his geology-oriented research on the effects derived by high pressure on powdered materials in order to explain the formation of various natural minerals [35, 41]. Although mechanochemistry started to be assumed and accepted as a distinct/separate subdiscipline of chemistry in 1919, a physical chemist and philosopher, the Nobel Laureate Friedrich Wilhelm Ostwald (Nobel prize in Chemistry, 1909, "in recognition of his work on catalysis and for his investigations into the fundamental principles governing chemical equilibria and rates of reaction") introduced it as a separate chemistry sub-discipline alongside electrochemistry, photochemistry, and thermochemistry [42]. Ostwald made this classification due to the fact that different types of energy are required in each sub-discipline.

### 1.4.2 Mechanistic Aspects on "How Ball Milling Works?"

Even nowadays, there is not a complete and comprehensive mechanistic picture regarding how ball milling and, in general, mechanochemistry works. This is also linked with the diversity of the utilized techniques/equipment (like mortar/pestle, mixer and planetary mills, glass vessel or tube disperser milling, etc. [3]) and the reaction types (dry or wet), conditions (gaseous atmosphere, temperature, etc.), and precursors (minerals, metal oxides, metals, chemicals, etc.). Several processes take place during the ball milling like heat and mass transfer.

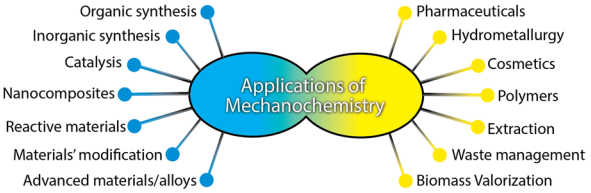


**Fig. 2** Applications of mechanochemistry

However, the most crucial driving force is believed to be the generation and relaxation of mechanical stress that have a direct effect on the crystalline lattices [3]. The theory of "hot spots" formation during ball milling is a widely accepted one [7]. Hot spots can be created by the cracking of crystals, resulting in local temperature (up to 5000 K) and pressure, electric fields up to 108 V/m, crack propagation with velocity close to that of sound (105 cm/s), and lifetimes for bond excitation around 100 fs [3, 43, 44]. These effects are analogues of those of US irradiation in a liquid, even though the formation of a hot spot results from the cavitation phenomena. And it is important that the high amount of added energy is localized microscopically, even nanoscopically, without affecting the macroscopic system to a great extent. This localized high amount of energy can lead to a diversity of consequences, such as lattice deformation, cleavage of bonds, or formation of radicals. And these phenomena cannot be achieved by other synthetic approaches in solution. Figure 2 presents the most important fields of mechanochemistry applications based on the report by Elena Boldyreva [43]. More mechanistic aspects and fields of application of mechanochemistry can also be found elsewhere [3, 7, 35, 44]. Even though Boldyreva did not consider US irradiation in her work, the latter can be utilized for the same fields and applications when a liquid phase is required. The rapid growth of the research interest around the application of mechanochemistry is due recent discovery of unique effects. By the correct utilization of these effects, it is feasible to obtain the desired nanostructured materials and enhance their crucial features by simultaneously eliminating the environmental footprint of the synthesis and avoiding the usage of high energy and hazardous and non-recyclable chemicals.

### 1.5 $TiO_2$: The Benchmark Semiconductor Photocatalyst

Titanium dioxide ($TiO_2$) can be regarded as one of the most popular semiconductor photocatalysts, for a wide range of applications; organic pollutant degradation, hydrogen production, solar cells, photocatalysis, etc. It combines high photo-activity for various reactions, high stability, low cost, and low toxicity for humans, animals, and the environment. Use of titanium dioxide started intensively in 1972, when Fujishima and Honda revealed photocatalytic water splitting by titania electrodes [45]. Since then, numerous articles have focused on the use of $TiO_2$ and its composites for green-oriented heterogeneous catalysis, like valorization of biomass and upgrading of obtained chemicals [1, 46, 47].

Another important property of titanium dioxide is its superhydrophilicity that is crucial for solar fuel production and environmental remediation applications [48]. However, one crucial drawback arises due to the fact that $TiO_2$ has a wide bandgap

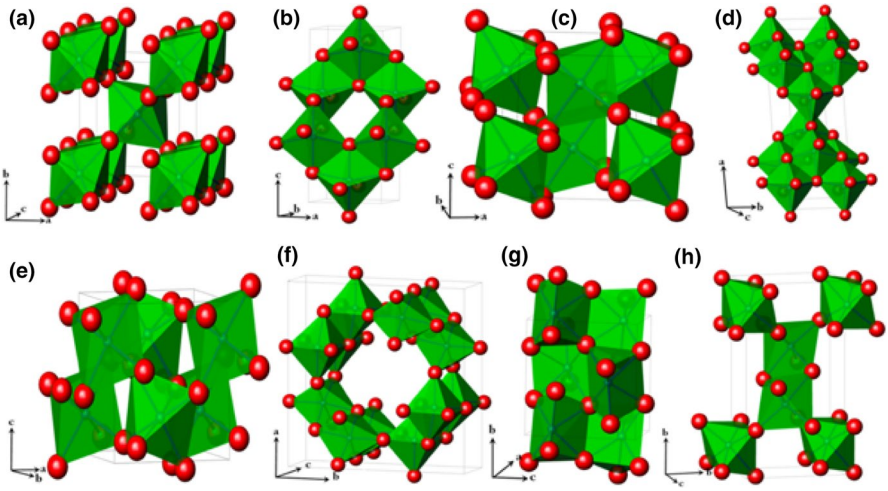


**Fig. 3** Crystal structures of rutile (**a**), anatase (**b**), bronze (**c**), brookite (**d**), columbite (**e**), hollandite (**f**), baddeleyite (**g**), and ramsdellite (**h**) phases. Reprinted with permission from [49]. Copyright (2015) Elsevier

ranging from 3.1 to 3.7 eV, and UV light irradiation is required in order to trigger the photoreactivity. Considering that solar light consists predominately of visible and infrared light, with ultraviolet light less than 5% of the total solar light, a persistent research effort is focused on narrowing of the bandgap and, as a result, increase of light absorption and photoreactivity under sunlight. Even though several polymorphs/crystal structures of $TiO_2$ exist [49], with the most important presented in Fig. 3, only a few of them have been studied and found promising for photocatalytic applications like biomass valorization [33, 50, 51]. The three most studied and stable crystalline phases of titanium oxide are anatase, brookite, and rutile, with the former one possessing the highest photocatalytic activity and the latter the highest stability [52]. Among the various commercially available forms of $TiO_2$, one of the most active and widely studied is Degussa P25, and, in many cases, it acts as a benchmark (industry standard) [53].

There are many reported methods for the synthesis of nanostructured $TiO_2$ materials. The sol–gel method is the most often applied method, but, unfortunately, it leads to amorphous nanomaterials, and, so, further treatment is needed to induce crystallization, like annealing. On the other hand, hydrothermal-based methods can promote the crystallinity and shape morphology formation, and can be used for larger scaled synthesis compared to the sol–gel method. Crystallinity in relation with the particle size is found to determine the photo-reactivity not only in the case of Ti-based catalyst [48, 54–57], but also for other materials like ZnO [58–60], $MnO_2$ [61], graphitic carbon nitride [5, 62–65], or other metal oxides/hydroxides [66–68]. However, the control of the final material's morphological features is related to a wide range of parameters during the synthesis.

Another important aspect in photocatalysis is the rate of the surface reactions. The structural (surface area and porosity) as well as the morphological features

(shape and size) play a key role in the catalysis rates, and, as a result, the engineering of these features is also important [47, 69–80]. Toward the above-mentioned direction, different strategies/approaches were followed for the nano-engineering of the $TiO_2$ toward key features/properties for application in catalysis. The most important strategies in order to positively trigger the photoreactivity are the following: (1) controlling the crystallographic nature; (2) introducing $Ti^{3+}$ species and lattice disorder; (3) doping with metal or non-metal; (4) decreasing the size of the particles to nanoscale; (5) engineering the shape to 0D, 1D, 2D, 3D, or amorphous; (6) decreasing the size of the particles; (7) chemical modification like hydroxylation/hydrogenation; (8) porosity enhancement; (9) narrowing the bandgap toward the visible range of light; (10) enhancing light absorption; and (11) limitation of $e^-/h^+$ recombination.

### 1.6 Our Approach to Organize this Article

The focus of the work herein is based on novel mechanochemical-assisted synthesis/modifications, such as US irradiation and ball milling, in which their utilization has led to beneficial effects in the enhancement of photocatalytic capability. Since the application of mechanochemistry has only lately been assumed and recognized as a useful process-intensification tool, in most works where US or ball milling were applied, the reports have predominately a materials point of view approach without studying a potential photocatalytic reaction. Additionally, the one-dimensional-inspired spatially ordered nanotubular-shaped titanate has gathered intense attention upon its discovery in 1995 [81]. Although the utilization of mechanochemistry in order to improve the synthesis and control specific features has been explored, the photocatalytic capabilities of these titanate nanotubes (TiNTBs) was studied in only a few of these reports. We believe that TiNTBs can display important photocatalyst behavior, and we actively work towards this direction. Based on the above and the available articles, we organized this article into two main parts/sections. In the first part, we collected the reports in which sonication was used in order to obtain nano-engineered materials with enhanced specific features for photocatalytic application, like light absorptivity, decreased bandgap, defects like surface oxygen vacancies, hydroxylation, porosity, etc. The second part is focused on the ball milling-based synthesis/modification approach. Each part is separated in two subsections. The first subsection is focused on zero-dimensional (0-D) photocatalysts, with an emphasis on how to promote the most vital of photochemistry features. In the second subsection, we collect all the research on the synthesis of one-dimensional (1-D) nanostructured titanate, like nanotubes (NTBs) and nanorods.

## 2 PART A—Sonication-Assisted Approaches

### 2.1 0-D Particles

#### 2.1.1 Increasing the Porosity

The supramolecular assembly sol–gel method using surfactant molecules as a template/structure-directing agent for the synthesis of mesoporous titania was reported firstly in 1995 by Antonelli and Ying [82]. The main drawback of the obtained hexagonally packed mesostructured $TiO_2$ was the presence of residual phosphorous from the alkyl phosphate surfactant. From then, different long-chain organic molecules were studied as phosphorus-free surfactants. In 2000, Wang et al. [83] reported a novel synthesis of mesoporous nanostructured titanate of a high porosity, by simultaneous ultrasonication during the synthesis (1.13 cm in diameter Ti horn, 20 kHz, 100 W/cm$^2$). An ethanolic solution of the organic amine and titanium isopropoxide was added slowly to a doubly distilled water, followed by aging for 6 h. The addition and the aging occurred under high-intensity ultrasonication, with the maximum temperature reaching 80 °C. The removal of the surfactant from the obtained powder by centrifugation was achieved by dilute ethanolic $HNO_3$ solution and washing with ethanol. The dried powder was also calcinated in a vacuum at 350 °C (8 h) or 450 °C (4 h). Three different long-chain organic amines (decylamine, dodecylamine, and octadecylamine) were studied as the structure-directing agents.

The result was spherical or globular particles between 50 and 200 nm as an aggregation of very small nanoparticles, as can be seen from the high-resolution transmission electron microscopy(HRTEM) image (Fig. 4). The X-ray diffraction (XRD) analysis showed an amorphous nature even after calcination at 350 °C, but the rise of the calcination temperature to 450 °C led to an anatase crystallinity. The surface areas after extraction, and calcination at 350 °C and 450 °C, were 853, 467, and 79 m$^2$/g, respectively. These values are high for metal oxides and higher than analogous titanate hexagonal mesoporous framework structures synthesized by hydrothermal and then thermal treatment with dodecylamine as a structure-directing agent (710 m$^2$/g) [83, 84]. The most interesting outcome was the that the obtained nanoparticles had a structure of disordered wormhole framework, rather than a long-ranged hexagonal structure. This kind of channel motif and the high surface area are ultimately important for catalytic application, due to the improved diffusion and the availability of the active reaction sites. Compared to various other reports for the synthesis of mesoporous $TiO_2$ nanoparticles, the benefits of this sonochemical method is the simplicity and rapid rate of synthesis, that leads also to nanoparticles of a high porosity. The authors linked the role of US irradiation to the accelerated condensation/polymerization of titanium hydroxide at the interface of the gas phase of the hotspots and the bulk solution.

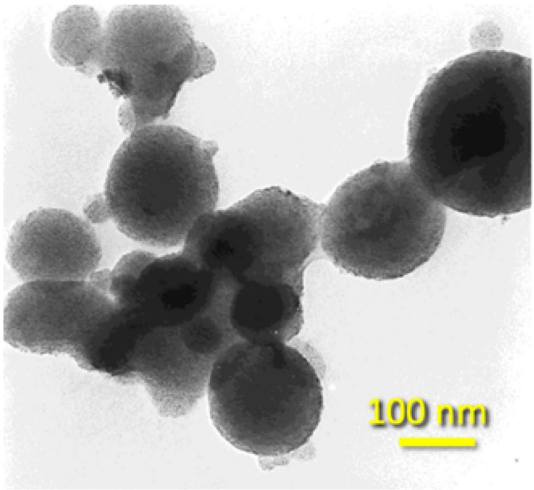


**Fig. 4** HRTEM images of the as sono-chemically prepared mesoporous titanium oxide with wormhole-like framework structures. Reprinted with permission from [83]. Copyright (2000) Wiley

### 2.1.2 Controlling the Crystallinity

In 2000, Huang et al. studied the role of US irradiation in the selective synthesis of anatase or rutile phases from different precursors and conditions [52]. The synthetic protocol was based on the addition of different precursors (TPT: tetraisopropyltitanate, TTC: titanium tetrachloride, or a mixture of TPT and TTC) in water under sonication by a directly immersed horn (20 kHz, 100 W/cm$^2$). The suspension was ultrasonic-aged for 3 h, with the temperature reaching 80 °C. The precipitates were obtained by centrifugation and subsequently washed with deionized water and ethanol, following by overnight vacuum drying. Compared to the sol–gel-derived materials that were amorphous prior to calcination, the samples obtained via US irradiation showed a high degree of crystallinity. Rutile-phased nanoparticles (crystallographic size based on the application of Scherrer's formula at the XRD: 8.2 nm) were obtained when TTC was used, and anatase phase (3.5 nm) in the case of TPT. The materials synthesized via US were also found to have relatively high surface areas, 103 m$^2$/g for the rutile phase and 201 m$^2$/g for the anatase phase. The TPT-derived sample (anatase) had a broad size distribution of mesopores (average of 5 nm), linked by the authors to the aggregation of nanoparticles. The rutile phase TTC-derived sample had a non-mesoporous nature.

When a mixture of TPT and TTC were used in a molar ratio of 63.4:36.6, a mixed anatase/rutile phase was determined. Analysis of the powder X-ray diffraction (PXRD) data revealed a crystallographic ratio of anatase to rutile phases of 47.6:52.4, suggesting that in the case of the mixture, part of the rutile phase formed at the expense of TPT. It should be pointed out that without US irradiation, the material obtained with the same mixture of precursors as above mixture was amorphous. The authors also studied the role of temperature. When the synthesis was conducted at 30 °C instead of 80 °C and TPT as precursor, the result was mixed brookite and anatase phases. On the contrary, when TTC was hydrolyzed under sonication at 10 °C, rutile phase was obtained. The role of pH was also studied, but not

in detail. When TPT was hydrolyzed under sonication at pH 0.7, the obtained sample of limited mass had a mix of rutile and anatase phases. Increasing the pH of the supernatant of the above synthesis to 8.6 and further sonication for 3 h led to a pure anatase phase. Based on all the above, it is obvious that even though US irradiation and temperature play a key role by promoting the crystallization, the pH can determine the finally crystallographic phase. Another outcome derived by the authors was that the hydrolysis of TPT in water is slower compared to TTC, resulting in a more homogeneous and partly condensed gel. The formation of a hotspot due to US waves inside the gel phase promotes the polycondensation of the Ti–OH species and the formation of a large number of seed nuclei, leading to smaller nanoparticles.

In 2001, Yu et al. [85] studied the effect of US irradiation (cleaner bath, 47 kHz, 120 $W_{elec.}$) as well as the role of the ethanol-to-water ratio during the hydrolysis upon precipitation of titanium tetraisopropoxide in pure water or mixed EtOH–$H_2O$ solution at different ratios, followed by in-air calcination at 500 °C for 1 h. The ratio of ethanol to water was found to play a key role in the crystallinity of the final powder, and, as a result, in the photocatalytic reactivity. While in pure aqueous solution, the obtained material had a mix of anatase and brookite phases (in a ratio of around 80:20); the addition of methanol led to the elimination of the brookite phase. The materials obtained without using methanol were found to possess a higher photoactivity against the oxidation of acetone in air compared to P25. On the contrary, the material with a solely anatase phase showed the lowest oxidative performance. The authors linked this to the fact that the presence of two crystallographic phases has a positive impact on the photocatalytic activity, by decreasing the combination of the photogenerated $e^-/h^+$ pairs. In 2010, Ghows et al. synthesized nanosized $TiO_2$ by hydrolysis of titanium tetra-isopropoxide in a solution of ethanol/water under low-intensity and high-frequency (500 kHz) sonication [86], although they did not study their photocatalytic properties. The crystalline phase and particle size were dependent on the ethanol-to-water ratio, US irradiation time, and temperature.

### 2.1.3 Altering the Surface Chemical Features and Bandgap

In 2011, Chen et al. [87] reported that the distortion and doping of the outer surface of $TiO_2$ nanoparticles by high-pressure and high-temperature hydrogenation led to an enhancement of the visible light absorption. Interestingly, and for the first time, the obtained $TiO_2$ powder did not have the characteristic white color, but a deep dark one. The reported synthesis of this material was conducted in two phases. In the first phase, titanium dioxide nanocrystals of an ~8-nm diameter were synthesized by a sol–gel method, using an organic template and acid (pluronic F127). The white powder obtained after calcination (500 °C, 6 h) underwent hydrogenation under a high-pressure (20 bars) $H_2$ atmosphere at ~ 200 °C for 5 days, resulting in a black powder, stable even after 1 year.

The HRTEM analysis revealed no shape alteration upon hydrogenation; however, an outer disordered layer around 1 nm in thickness appeared. The X-ray diffractogram of both white and black samples revealed the characteristic peaks of the anatase structure. The Raman spectrum of the white sample showed the six typical Raman-active modes of the anatase structure. The Raman spectrum of the

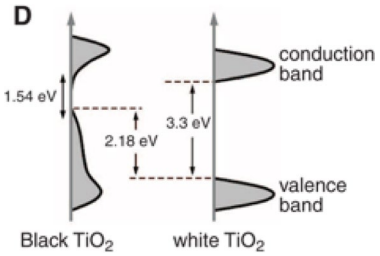


**Fig. 5** A schematic illustration of the density of states (DOS) of disorder-engineered black $TiO_2$ compared to that of the white $TiO_2$ precursor. Adapted with permission from [87]. Copyright (2011) American Association for the Advancement of Science

black sample revealed a broadening of the six typical Raman-active modes which were appeared in the white powder, and some additional new bands not linked to any of the three classic polymorphs of $TiO_2$. The X-ray photoelectron spectroscopy (XPS) analysis revealed an almost identical and impurity-free bonding environment for Ti. On the contrary, the hydrogenation also resulted in a new O 1s peak (at 530.9 eV) which was attributed by the authors to the formation of Ti–OH moieties. Since the dangling bonds tends to attract hydrogen, the authors expected that the H doping occurred predominately in the outer disordered layer where more dangling bonds exist compared to the inner crystalline core. The bandgap of the non-hydrogenated materials was determined by diffuse reflectance as 3.3 eV (slightly higher than bulk anatase). The black $TiO_2$ showed a dramatically narrower bandgap , while the onset of the optical absorption started from ~ 1200 nm (1.0 eV). The authors linked this to the "band tail states" phenomena, where the valence and conduction bands narrow. The density of states (DOS) of the black sample compared to the white one can be seen in Fig. 5. The photocatalytic activity against methylene blue dye was found to be faster by ~ 7.5 folds under solar irradiation, and the photo-activity was found to be stable even after eight cycles. More interestingly, the black titania sample was found capable of photocatalytic hydrogen production from water under sunlight, with a rate two folds higher than the best semiconductor catalysts at that time. The non-hydrogenated sample was not found photoreactive for water splitting, even after loading with Pt. The H production was repeatable for more than 20 cycles. The authors showed that the hydrogenated $TiO_2$ did not act as an H reservoir, since 40 mg of $H_2$ were formed after 100 h of irradiation, with the sample having around 0.05 mg of hydrogen.

In 2012, Osorio-Vargas et al. studied the effect of low-frequency US irradiation (20 kHz, 1.2 W/mL) on P25 [88]. Based on electron spin resonance (ESR) measurements, they reported evidence to support the formation of oxygen vacancies for the obtained sample after 6 h of irradiation. These vacancies can be responsible for enhance visible light absorption, and also for the obtained grey-shaded color, although the photoreactivity was not studied. These surface chemistry alterations were assigned to the shock waves from the cavitation phenomena and high-velocity interparticle collisions.

In 2015, Fan et al. utilized ultrasonication in order to synthesize amorphous and porous hydroxylated black $TiO_2$ [89], avoiding the harsh and expensive synthesis by hydrogenation at high pressure (20 bars) and temperature (200 °C). The pivotal role of US waves during the synthesis was determined by varying the irradiation

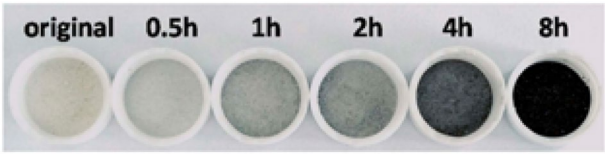


**Fig. 6** The powders obtained after different ultrasound irradiation duration. Reprinted with permission from [89]. Copyright (2015) Springer Nature

duration (0.5–8 h), leading to different shades of blackness. At the first step of synthesis, titanium sulfate [$Ti(SO_4)_2$] and ammonia water were inserted in aqueous phase inside an ice-water bath in order to control the reaction rate (2 h, under magnetic stirring). After centrifugation and US washing (25 kHz, 100 W, 20 min) by deionized water, the dispersion was treated with high-power US irradiation (25 kHz, 1500 W/100 mL) using a probe. The synthesis was conducted at 80 °C under different US irradiation durations; 0.5, 1, 2, 4, and 8 h. Afterward, the obtained materials were dried at 80 °C. The degree of the black shade was increased by extending the US irradiation (Fig. 6). After 8 h of US exposure, the obtained powder had a deep black color. It was pointed out that by the application of lower-intensity US irradiation, no powder with a black shade was obtained.

The X-ray diffractograms of all samples were almost identical, revealing no reflections as a result of the amorphous nature. Identical Ti 2*p3/2* and Ti 2*p1/2* peaks were also found in the XPS spectra, and no shifting, widening, or narrowing was observed, linked to the $Ti^{4+}$ of the Ti–O bonds. Since no $Ti^{3+}$ moieties exist in the matrix, all the obtained samples, regardless the color, were assumed as amorphous $TiO_2$. The XPS analysis also showed the absence of other elements, rather than Ti and O, independent of the US irradiation and duration. The TEM and HRTEM images (Fig. 7) revealed that the obtained materials had an absolute disorder and amorphous structure, with or without US treatment. The same research team reported in a prior work the synthesis of hydroxylated amorphous and disordered $TiO_2$ nanomaterials of different color shades [90]. The only difference was that instead of US irradiation, the obtained intermediate white powders were thermally treated in a muffle for 3 h (heating rate ~ 20 °C/min) at different temperatures; 200–800 °C. These nanomaterials, as also in the case of those reported by Chen et al. [87], had a specific structure: an anatase nano-core/shell surrounded by a disordered and amorphous hydroxylated phase. Contrarily, the US treatment led to core-free pure amorphous $TiO_2$ nanocrystals. In order to exclude the possibility of the blackness being associated with N doping, NaOH was used as a base instead of ammonia, and the obtained materials showed similar blackness increment by the extension of US irradiation.

The initially white and all ultrasonictreated samples darker in color showed similarly shaped O1s XPS spectra. The peak was deconvoluted to two symmetric peaks, one assigned to Ti–O bonds (~ 530 eV) and the other to Ti–OH (530.9–532 eV). However,, the Ti–OH/Ti–O ratio of Gauss peaks was increased by increasing the US treatment duration. The amorphous white $TiO_2$ had a

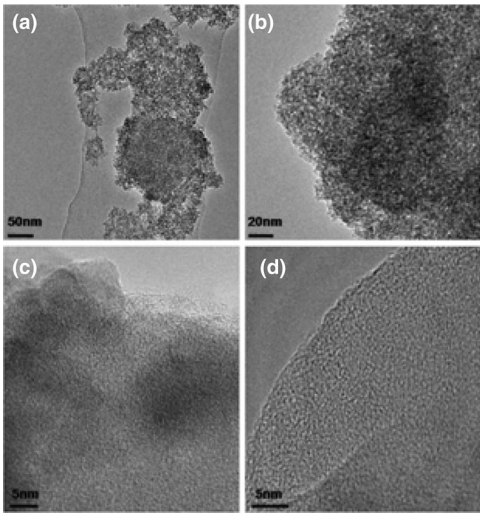


**Fig. 7** TEM and HRTEM images of non-ultrasound-treated white $TiO_2$ (**a**, **c**) and amorphous hydroxylated black $TiO_2$ obtained after 8 h of ultrasonication (**b**, **d**). Reprinted with permission from [89]. Copyright (2015) Springer Nature

Ti–OH/Ti–O ratio of 0.73, while for the black sample, the ratio was more than double (1.60). The authors determined the hydroxylation degree and assumed a molecular formula of $TiO_{2-x}(OH)_{2x}$, where "$x$" represents the hydroxylation extension. The reported molecular formulas were $TiO_{1.156}(OH)_{0.844}$ for the white powder and $TiO_{0.768}(OH)_{1.232}$ for the black sample. Calcination of all colored samples at 800 °C until a constant weight led to white powders, as a result of the transformation of Ti–OH to Ti–O. Based on all the above-mentioned results, it was concluded that the high-power US irradiation duration had a direct correlation to the hydroxylation and amorphism.

The increase of the hydroxylation and amorphism as a result of longer ultrasonic irradiation had additional positive impact on the desired, and ultimately key, features in catalysis due to improvement of light harvesting; the structural and optical features. The absorbance intensity through the whole visible and near-infrared regions was improved by the increase of the ultrasonication duration, while the bandgap was decreasing. The white and the black samples had a bandgap of 3.37 and 3.11 eV, respectively. The density of states (DOS) constructed by the optical absorbance and valance band XPS spectra (Fig. 8) showed that the narrowing of the bandgap was assigned to electronic structure alterations due to orbital overlapping, and the blue-shift of the valence band maximum towards the Fermi energy.

The increased porosity is also an important factor for photocatalytic application, since it enhances the reaction rates as a result of improved diffusion of the reactants and the availability of the active sites. For all studied samples, the obtained type IV nitrogen sorption isotherms with type H2 hysteresis loops revealed the existence of meso-pores/voids [91], resulted from the interstitial spaces between the nanoparticles, as was reported in various cases [80]. The lowest porosity values were found for the non-US-treated white powder; a surface area of 166.43 $m^2/g$ and total pore volume of 0.109 $cm^3/g$. The US irradiation gave rise to the microporosity due to the hydroxylation of $TiO_2$, as it was reported in other cases [92]. The black sample

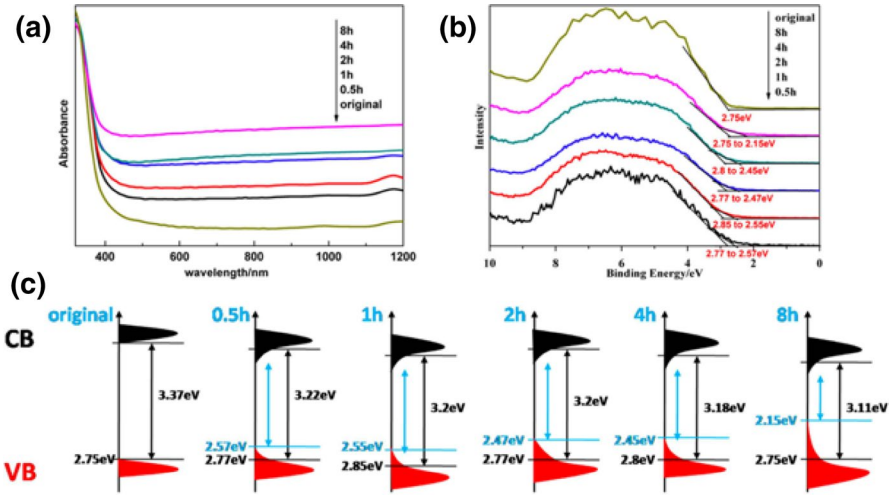


**Fig. 8** UV–Vis–IR absorbance spectroscopy (**a**), valance band XPS spectra (**b**), and a schematic illustration of density of states (DOS) of the original samples and amorphous hydroxylated samples ultrasonicated for different durations. The blue and black arrows indicate the bandgaps after and before localized band-bending, respectively. Reprinted with permission from [89]. Copyright (2015) Springer Nature

US-irradiated for 8 h showed the highest structural parameters, which were double compared to the white sample (surface area: 329 $m^2/g$ and total pore volume: 0.251 $cm^3/g$).

The evaluation of the photocatalytic capability of the samples was performed by monitoring the decomposition/removal of acid fuchsin (AF) in aqueous solution. Since the materials were porous, the removal/reactivity in the dark was evaluated in detail prior the evaluation of photocatalytic performance. It was found that the black nanomaterial had an almost three times higher removal capability in the dark compared than the white one, due to the higher surface area and pore volume. The analysis of the interactions (by eliminating the effect of physical adsorption) showed that the US-assisted synthesis led to samples that possess an improved solar- and the visible-light-driven photocatalytic reactivity. The first-order rate constant obtained by the Langmuir–Hinshelwood model for the black sample was 5.8 and 7.2 times higher under solar and visible light irradiation, respectively, compared to the non-US-treated white sample. The decomposition capability was linked to the formation of hydroxyl radicals. The fact that the photocatalytic reactivity improvement was more pronounced in the case of visible light was linked to the enhanced light utilization/harvesting, photo-response range, and the narrowing of the bandgap. Photoluminescence tests showed that the increase of the ultrasonication duration led to a decrement of the photo-generated electrons and holes pairs, with the latter being trapped at the disordered phase.

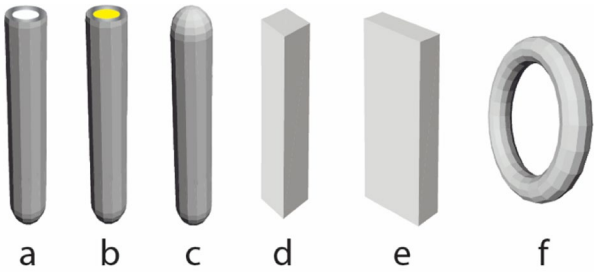


**Fig. 9** Schematic illustrations of the most widely synthesized and reported titanium oxide nanoscaled morphologies: open-end nanotube (**a**), core–shell nanotube (**b**), nanorod (**c**), square or rectangular nanorod/belt (**d**, **e**), and nanoring (**f**)

## 2.2 1-D Particles

### 2.2.1 1-D Titanium Oxide and Titania

In the literature, various different names/terminologies are used for the characterization of the structure and shape of the 1-D synthesized materials, like fibers, whiskers, nanotubules, fibrils, nanocable, rods, nanowires, belts, since the definition and nomenclature are not well stablished [93]. The geometrical shapes of the titanium oxides that are more widely accepted, reported as a characteristic based on electron microscopy images, and herein used, are collected in Fig. 9. In general, the most important shapes are the open-end NTB (a), the core–shell NTB, the nanorod (c), the square or rectangular nanorod/belt (d, e), and the nanoring (f) [93].

The first report of 1-D $TiO_2$ NTBs was by Patrick Hoyer in 1995 [81], who used a poly(methyl methacrylate) (PMMA) mold/template for the electrochemical deposition/growth of the titania NTBs. After the dissolution of the polymer, the obtain material consisted of poorly organized arrays of amorphous TiNTBs. The diameter of these NTBs was in the range of 140–180 nm, with an inner hole diameter of 30–50 nm and wall diameter of 30–50 nm. A 45° view of the cross section of the lower part of the amorphous tubes (after the removal of the upper part of the NTBs) is presented in Fig. 10. The electrochemical synthesis is out of the scope of this work. A detailed review article for the electrochemical formation of self-organized $TiO_2$ NTBs was published by Roy et al. [94].

The fascinating TiNTBs were bulkily and template-free firstly obtained in a powder form via the innovative work of Kasuga et al. in 1998 [95]. TiNTBs with a small diameter (Fig. 11i) were synthesized from the conversion of $TiO_2$ (mixed rutile and anatase) by a soft chemical method; hydrothermal treatment (110 °C, 20 h) in a strongly basic environment (10 M NaOH). They showed by TEM how the treatment with diluted HCl can lead to nanotubular structures and of high specific surface area, up to 257 $m^2/g$. Peng's group analyzed in a series of articles in between 2001 and 2003 [96–99] the crystallographic structure of the hydrothermally obtained TiNTBs, and assigned it to trititanate $H_2Ti_3O_7$. They also presented the catalytic role of NaOH and how the NTBs are formed by the rolling of the intermediately formed

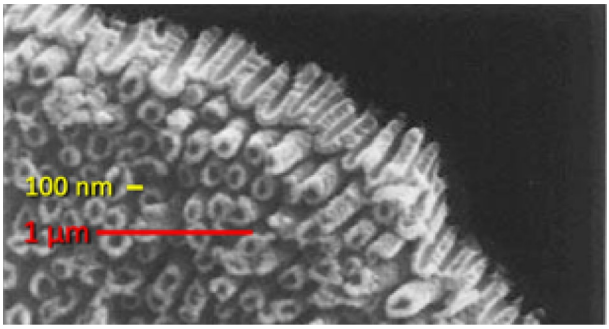


**Fig. 10** SEM pictures of the cross section of the as-prepared film of titania (with the upper part of the tubes removed). (Adapted from Fig. 3 of [81]). Reprinted with permission from [81]. Copyright (1996) American Chemical Society

nanosheets (Fig. 11ii). In 2004, Suzuki and Yoshikawa expanded the analysis by proposing that the presence of water molecules is crucial [100], expressing the formula as $H_2Ti_3O_7.nH_2O$, and showed that these moieties of the crystallographic water play a role in the interlayer spacing of titanate layers of the NTB's wall.

In general, this synthetic process involves two main steps, the first being a conventional solid-state reaction between $TiO_2$ and sodium ions in basic solution, forming layered structures peeled from the initial particles. The second step involves the ion exchange during the acid treatment, HCl in almost all reported cases. Two factors are important regarding the formation of the alkali metal stabilized nanotubes: (1) how the nanosheets are formed from the spherical (in most cases) nanoparticles, and (2) how the nanosheets are converted to NTBs. Regarding the first aspect, Nakahira et al. showed by TEM observation (Fig. 12i) in 2010 that the formation by surface exfoliation of the nanosheets and their rolling/wrapping to NTBs take place on the surface, using as raw material an anatase-type titanium dioxide, and they proposed the entire process by various characterizations [102]. Bavykin et al. presented three different possible mechanisms of the conversion of the nanosheets to open-end multi-wall NTB, resulting in differently structured tubular shapes (Fig. 12ii) [103].

After the first reports of the TiNTBs, an intense research effort was focused on tuning different parameters during synthesis in order to control the structural and morphological features, the homogeneity and purity of the formed TiNTBs, as well as to decrease the synthesis temperature and duration [100, 102–110]. However, some arguments were derived. More details regarding titania NTBs obtained by hydrothermal-based synthesis can be found in the review article reported in 2011 by Wong et al. [111]. In many of the reports regarding the synthesis of the 1-D nanotubular structures, US irradiation was applied at different stages of the process, but without analyzing the possible role. It is feasible to believe that US led to specific effects that were not explored. Sonication can also help the characterization and separation of the TiNTBs. Interestingly, Bavykin et al. showed that US irradiation can be beneficial in order to distinguish the nature of the high observed pore volume by separating the agglomerates into individual NTBs [103].

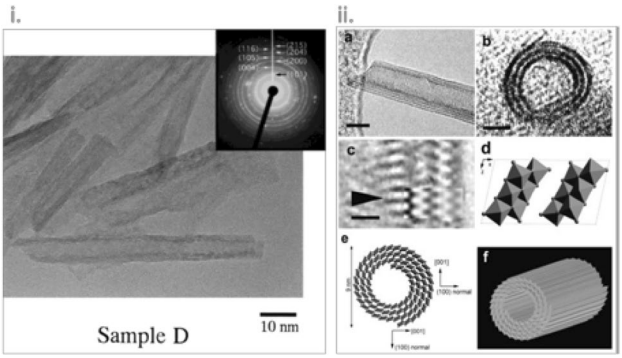


**Fig. 11** **i** TEM image and SAED pattern of titanate nanotubes hydrothermally synthesized the for first time by Kasuga et al.; **ii**: **a** HRTEM image showing a nanotube with an open end and three or four layers at the walls (scale bar 6 nm); **b** HRTEM image of the cross section of a three-layered wall nanotube (scale bar: 3 nm); **c** enlarged HRTEM image (scale bar: 1 nm); **d** a structure model of a single unit cell of $H_2Ti_3O_7$ ([010] projection); **e** schematic illustration of the nanotube's structure; **f** 3-D drawing of a titanate nanotube. Adapted with permission from [97, 101], respectively. Copyright (1999) and (2002) Wiley

The focus of the following part is on how the sonication can play a vital role for the manipulation of the TiNTBs' important factors like size, shape, porosity, peeling of the nanosheets, and more, as well as how the process can be achieved faster with a more environmental and energy-friendly manner. The photocatalytic activities and the involved mechanisms, if reported, are also introduced and discussed.

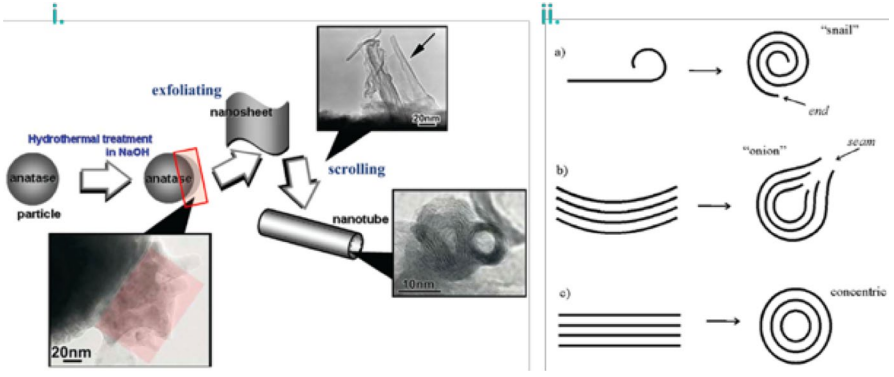


**Fig. 12** **i** A schematic collective scheme for the exfoliation and wrapping/scrolling of the formed titanate nano-sheets leading to the nanotubular particles, supported by TEM observations; **ii** a schematic representation showing the possible mechanisms for the formation of the nanotubes. Adapted with permission from [102, 103]. Copyright (2010) American Chemical Society and (2004) RSC, respectively

### 2.2.2 1D Titania by Ultrasound Irradiation

In 2001, Zhu et al. [112] demonstrated that the utilization of low-frequency US can promote the formation of 1-D titanate nanoparticles. The one-pot synthesis of the

whiskers and nanorods was based on the sonication of synthesized titania nanoparticles in strongly basic solution (NaOH, 10 M), following by washing with dilute $HNO_3$ (0.1 M) and deionized water and vacuum drying. Compared to other methods used for the synthesis of 1-D structured titania (template synthesis, supra-molecular assembles, hydrothermal synthesis, and inductive synthesis), this synthetic approach taking place in a one-pot synthesis is faster, while avoiding the use and removal step of the templates and the need of calcination for crystallization as the last step.

The used synthesized $TiO_2$ nanoparticles as precursors were prepared by hydrolysis of titanium butoxide, followed by calcination at 650 °C for 1 h. The average size of them was around 20 nm, while the crystallographic composition was 17% anatase and 83% rutile. For the synthesis of the whiskers, synthesized titanium oxide nanoparticles were dispersed in the basic aqueous solution inside a Teflon vessel. The mixture was ultrasonicated for 80 min (direct immersion of Ti-horn, 560 $W_{elec.}$, frequency not specified but probably in the low-frequency range, 20–80 kHz). The temperature during the synthesis was 80 °C.

Then the mixture after sonication was washed with diluted $HNO_3$ for 2 h and with deionized water for 6 h. The obtained particles had a slender sheet structure of a 60-nm diameter and a length around 1 μm. The interesting outcome arises from the elemental stoichiometry analysis, which was found to be $H_3Ti_3O_{7.5}$. The bands at ~ 3400 and ~ 1630 $cm^{-1}$ at the IR spectrum were linked to the stretching vibrations of the O–H bond and to bending vibration of H–O–H, revealing the presence of water. Since the XRD pattern matched with that of $H_2Ti_3O_7$ [113], and taking into consideration the thermogravimetric results, the product was assigned from the authors as $H_2Ti_3O_7.0.5H_2O$. Further washing of the product with water for 8 h led to nano-whisker arrays of a 5-nm diameter. The X-ray diffractogram revealed that the crystallographic phase changed to $TiO_2$ (B) [114] (Fig. 13).

For the preparation of the NTBs, the mixture was treated with half the US power (280 $W_{elec.}$) for 60 min, and afterward, the Teflon vessel was maintained in an oil bath at 110 °C for 4 h. The washing was with $HNO_3$ (0.1 M, 2 h) and deionized water (14 h). The obtained NTBs had a 5-nm diameter and 200–300-nm length. The XRD analysis revealed that the crystallographic phase was an intermediate between $H_2Ti_3O_7{\cdot}0.5H_2O$ and $TiO_2$ (B). No Na was detected at the elemental analysis, while the ratio of Ti to O was 1:2.

The proposed mechanism of the whisker formation was based initially on the US-assisted reaction of the base that leads to the cleavage of some Ti–O–Ti bonds. The formed layered titanate lattices have octahedral form with alkali metal ions to occupy the interlayered regions. During the washing with acid and water, ion exchange and dehydration occur, resulting to $H_2Ti_3O_7{\cdot}0.5H_2O$. Extended dehydration by water washing promotes the transformation to titanate bronze. The role of US is vital since it promotes the reaction between the raw nanoparticles and the base, as well as controls the oriented growth. The synthesis is faster by the application of US compared to the reported hydrothermal methods of nanorod formation. It is worth mentioning that without ultrasonication, no whiskers were obtained. A lower US irradiation power and the hydrothermal treatment promotes the formation of bigger titanate sheets and the exfoliation of nanosheets. The latter roll into NTBs during the washing due to the removal of the ions and, as a result, to alterations

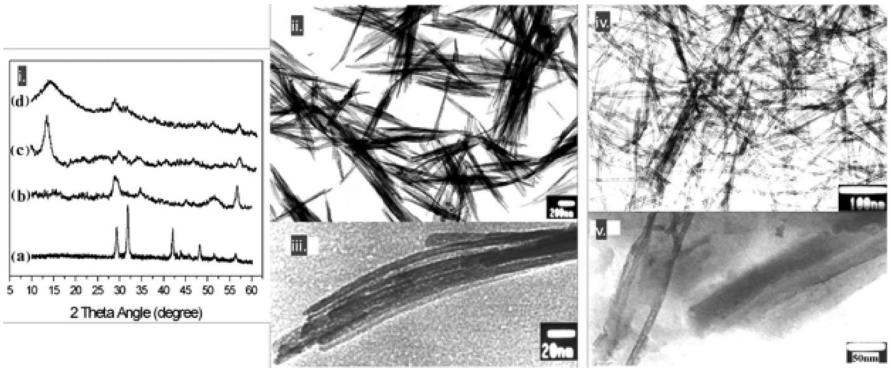


**Fig. 13** **i**: XRD patterns of titania particle precursors (a), titania whiskers (b), $H_2Ti_8O_{17}$ whiskers (c), and nanotubes (d); TEM images of titanate (**ii**) and $TiO_2$ whiskers (**iii**), titania nanotubes (**iv**), and sample obtained by thermal treatment (4 h, 110 °C) of the sonicated products followed by washing with water for 5 min (**v**). Adapted with permission from [115]. Copyright (2005) American Chemical Society

of the electrostatic forces/equilibria. Even though the above US-assisted hydrothermal approach successfully led to the preparation of NTBs significantly faster and easily compared to the hydrothermal synthesis, there is a drawback. The synthesis of the precursor starting with titanium butoxide hydrolysis is time-consuming and complex.

In 2005, Joo et al. [115] reported the synthesis of $TiO_2$ nanorods of a diameter and length of 3.4 and 38 nm, respectively, by a nonhydrolytic ester elimination reaction between titanium(IV) isopropoxide (TTIP) and oleic acid [OA, $CH_3(CH_2)_7CH{=}CH(CH_2)_7COOH$]. The latter monosaturated fatty acid is among the most common fatty acids in nature, produced both from vegetables and animals, and in this work, it was utilized as surfactant and shape stabilizer during the synthesis. Even though the authors concluded that the obtained crystallographic phase was of anatase, they did not report the region of the XRD for angles lower than 20°. In the following preparation method, TTIP was added to OA, and the suspension was heated gradually until 270 °C within 20 min and was kept at this temperature for 2 h. The initial clear solution of a yellow shade turned progressively to white. The yield was around 70% wt, and the white powder consisted of nanorods and quasi-spherical nanoparticles ~3-nm diameter (Fig. 14a, b). Interestingly, the authors were able to separate the nanorods by conducting a size-selective precipitation from a hexane/ethanol solution (Fig. 14c). They also showed that the nanorods' diameter could be controlled by adding different amounts of 1-hexadexylamine. Sonication for 30 min (experimental conditions not specified) was applied for the removal of the surfactant after the treatment of the powder with superhydride solution (lithium triethylborohydride in THF), but the effect of US was not explored. The finally obtained nanorods presented a specific surface area of 198 $m^2/g$ and they were highly dispersible in water, a fact of a paramount importance for real-life applications. The estimated bandgap of the nanorods was 3.33 eV, a value higher than that of 3.2 eV of the bulk anatase, due to quantum size effect. Compared to commercial $TiO_2$ P25, the obtained nanorods were found to possess a higher photocatalytic inactivation

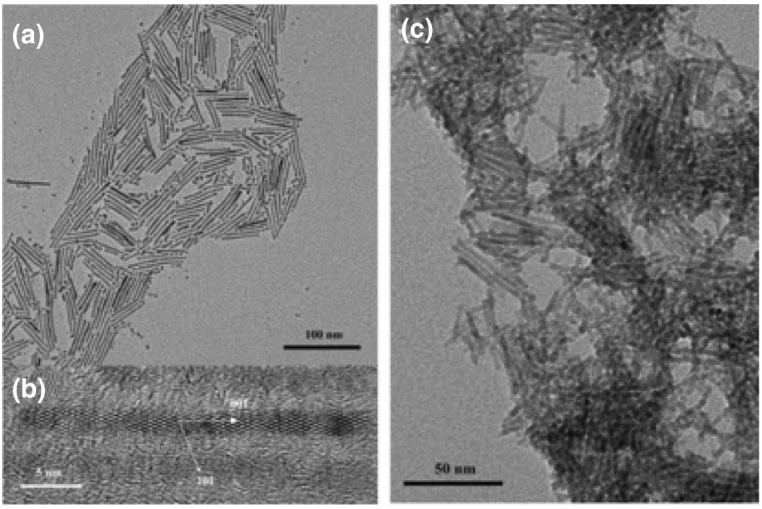


**Fig. 14** TEM and HRTEM images of the as-synthesized $TiO_2$ nanocrystals prior the size-selective separation (**a**, **b**) and TEM image of the final $TiO_2$ nanorods (**c**). Reprinted with permission from [115]. Copyright (2005) American Chemical Society

capability against *E. coli*, a fact that was assigned by the authors to the increased bandgap, surface area, and amount of surface hydroxyl groups. The improved and faster inactivation performance for the nanorods was linked to the elevated hydroxyl radical formation.

Since the morphological and structural features of TiNTBs (size and porosity) can be controlled, the application of US irradiation towards the increment of these features gained more attention. Ma et al. [116] reported in 2006 the synthesis of longer NTBs with a smaller diameter by a combined sonication-hydrothermal approach and using as precursor the commercial $TiO_2$ P25. Their approach was based on dispersing the commercial powder in a Teflon vessel filled with NaOH aqueous solution (10 M). Using an immersed titanium horn (probably low-frequency, not specified), the suspension was sonicated at 70 °C under different sonication powers (100, 280, and 380 $W_{elec.}$) and varying also the duration (15, 30, and 60 min). The vessel was placed in a stainless-steel autoclave for hydrothermal treatment for 4 h at 110 °C. The obtained precipitate was washed with HCl (0.1 M) and deionized water until an acidic pH, centrifuged, and dried under vacuum. The role of the precursor on the size of the NTBs was determined by using different commercial $TiO_2$ precursors.

The hydrothermal treatment of the nanospherically shaped P25 particles of an average size of ~ 30 nm without ultrasonicated pre-treatment led to minimal particle shape alteration. Sonication for 1 h prior the hydrothermal treatment with powers of 100 and 280 $W_{elec.}$ resulted in sheet and fibrous morphologies, respectively. A typical tubular morphology was achieved (diameter: 9–14 nm and length: 100–600 nm) by sonication at a higher power (380 $W_{elec.}$), revealing that the sonication, as well its power, plays a key role in the desired transformation to TiNTBs. TEM images of

the initial $TiO_2$ P25 and the TiNTBs produced by combining high-energy sonication and hydrothermal treatment can be seen in Fig. 15.

The crystallinity and the chemical composition of the nanorods were investigated by XRD and energy-dispersive spectroscopy (EDS) analysis. It was concluded that the chemical composition was $H_2Ti_4O_9.H_2O$ (JCPDS 36-0655), while traces of rutile fractions were also observed. Considering that the $TiO_2$ P25 consisted of 70% anatase phase and around 30% rutile phase, the transformation of the latter phase is preferable, while the former type is more stable under the hydrothermal treatment conditions. The EDS elemental analysis showed the absolute absence of Na.

The authors also studied the effect of the higher sonication power (380 W) without the hydrothermal and acid treatment. 15 min of US irradiation did not reveal the ability to alter the shape of the spherical particles. Increase of the irradiation time to 30 min led to swelled nanoparticles with an average diameter of 100 nm, probably as a result of the spherical particles merging. By increasing the duration of irradiation to 60 min, the observed morphology was found to be nanorods like, with lengths in between 100 and 300 nm. By hydrothermal and acidic treatment after the 60 min of US irradiation, the length of the nanorod-like particles increased up to 600 nm. Additionally, the diameter of the tubes was also smaller, but the shape homogeneity was not so perfect. Based on these observations, it can be proposed that the US effects can originate the reaction of the $TiO_2$ nanoparticles with the base, by promoting the cleavage of the Ti–O–Ti lattice bond and the intercalation of $Na^+$ at the lattice. The spherical forms are swollen and transformed to nanorods by increasing their length. Calcination at 300 and 450 °C of the sample obtained after the two-step process was not accompanied with notable shape alterations (Fig. 15c, d). On the contrary, calcination at 600 °C led to morphology transformation of the hollow tubular structures to rod-like structured nanoparticles (Fig. 15e).

Interesting outcomes regarding the vital role of the precursor's particle size were derived by using two other commercial $TiO_2$ powders instead of P25. When the size of the initial particles was around 10 nm (Hombikat UV100, Fig. 16a), the formed NTBs had inner and outer diameters and lengths of 3–6, 7–10, and up to 400 nm, respectively (Fig. 16b). When particles of a bigger average size of 200 nm (BCC100, Fig. 16c) were used as precursor, instead of tubular-shaped particles, sheet-like structures with rolled edges were obtained together with untransformed particles that were slightly changed in size and shape (Fig. 16d). This was linked to the fact that the formed sheet-like structures cannot transform/roll to tubes, perhaps due to a hindrance effect by the larger particles.

Tanthapanichakoon and his colleagues showed and analyzed how the ultrasonication pretreatment can influence controllably the length of the titania NTBs [117, 118]. Interestingly, they used a commercial precursor (KISHIDA) of a low specific surface area (8 $m^2/g$) and relatively large particles (400 nm) compared to the previous reports. By using a titanium horn (probably low-frequency, not specified in the article), the suspension of $TiO_2$ in a 10 M NaOH aqueous solution was sonicated prior the hydrothermal treatment for 8 min with different supplied powers, from 0 to 38.1 W. After thermal treatment for 3 days at 150 °C, the obtained suspension was treated/washed with HCl and $H_2O$. TEM analysis revealed that no US irradiation led to TiNTBs (herein referred to as short) with multilayered walls (2–6 layers

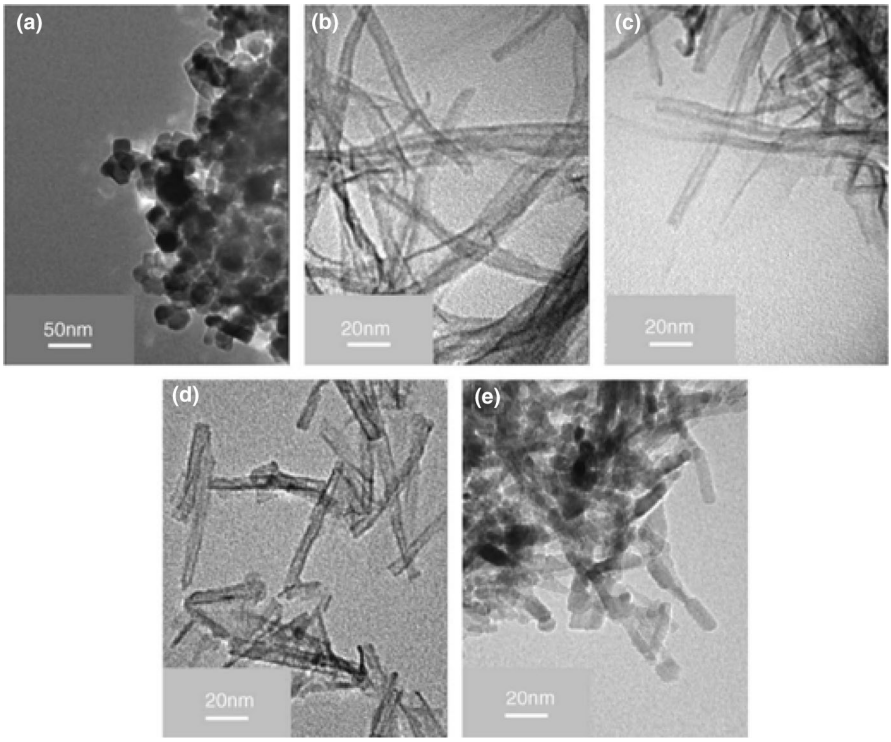


**Fig. 15** TEM images of $TiO_2$ P25 precursors (**a**), titanate nanotubes as received (**b**), after calcination at 300 °C (**c**), at 450 °C (**d**), and 600 °C (**e**). Adapted with permission from [116]. Copyright (2006) Elsevier

and ~ 0.8-nm interlayer spacing), diameters from 4–6 nm, and lengths between 30 and 200 nm. Sonication by two different powers, of 7.6 and 38.1 W, led to increase of the TiNTBs' diameter. The majority of the NTBs had a length above 300 nm, while the diameter was in the same range with that of the short ones. Based on the previous analysis by XRD of the *d*-spacing between the adjacent layers of the tube walls by Suzuki and Yoshikawa, the authors concluded that the US irradiation and the resulted increase of the length was not accompanied with an interlayer spacing change. Additionally, the strong intensity diffractions of the initial $TiO_2$ (anatase phase) were totally diminish in all synthesized TiNTBs.

The dynamic light scattering (DLS) results showed average sizes of 53, 490, and 1760 nm for the samples prepared under 0, 7.6, and 38.1 W, respectively. Additionally, the size distribution was very narrow in the case without US irradiation, and the distribution was dramatically increased by increment of the applied US power. The formation of NTBs in size many folds higher the pristine particles can be linked to bigger peeled nanosheets prior the rolling, and/or to the connection of the formed tubes. An increasing trend was found between the specific surface area ($S_{BET}$) and the power of US irradiation. The raw powder had an $S_{BET}$ of 8 $m^2/g$, and the short

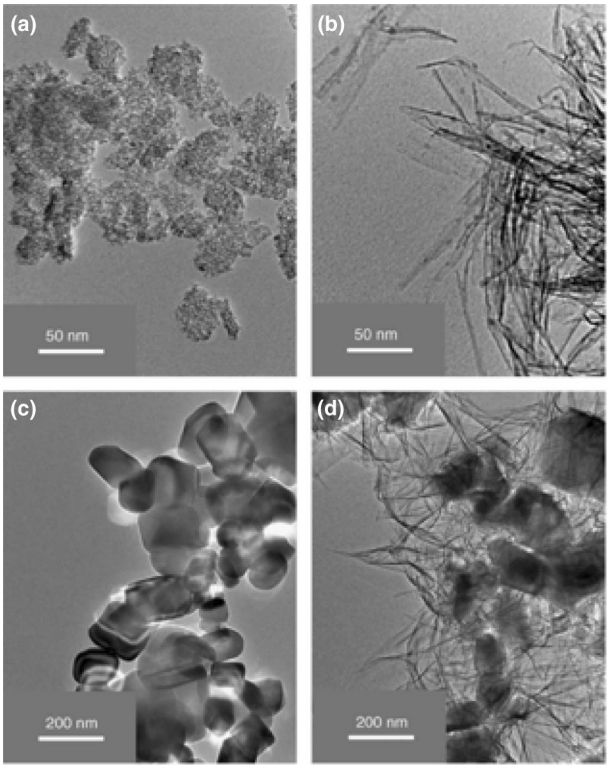


**Fig. 16** TEM images of $TiO_2$ Hombikat UV100 precursor (**a**), titanate nanotubes derived by sonication-hydrothermal treatment of Hombikat UV100 (**b**), $TiO_2$ BCC100 precursor (**c**), and sample obtained from BCC100 (**d**). Adapted with permission from [116]. Copyright (2006) Elsevier

NTBs 179 $m^2$/g. The US wave exposure at the pretreatment stage led to $S_{BET}$ of 258 and 245 $m^2$/g, for US power of 7.6 and 38.1 W, respectively. The positive effect of ultrasonication is via the enhancement of the de-aggregation of the particles, resulting in the peeling thorough swelling of large nanosheets that role to NTBs [118]. Without US waves, the size of the peeled nanosheets and, as a result, the size of the formed NTBs is smaller.

The same research team studied (in 2009) the effect of different preparation variables and combinations like particles size of the raw $TiO_2$ (400 nm and 1 μm), temperature during the synthesis (90–180 °C), and sonication power, with valuable conclusions on how these variables can adjust the morphological and structural features [117]. The hydrothermal treatment at 150 °C without sonication of the commercial $TiO_2$ particles of size ~ 400 nm led to NTBs of an average length of 79 nm and a specific surface of 179 $m^2$/g. The respective values were 143 nm and 118 $m^2$/g when the largest (1 μm) raw particles were used. This was linked to the formation of bigger but less in number intermediate sheets during the peeling. By studying the effect of different temperatures (90, 120, 150, and 180 °C), it was concluded that the

transformation of titanium dioxide to titanate was complete even at 120 °C. However, increase of the temperature to 180 °C led to a shift of the characteristic diffraction at around 10° 2$\theta$ to a higher angler (~ 12°), suggesting a narrow interlayer spacing between the layers of walls. Suzuki and Yoshikawa assigned the characteristic XRD reflection peak at $2\theta = \sim 10°$ of the hydrothermally synthesized $H_2Ti_3O_7.nH_2O$ NTBs to an interlayer distance of 0.92 nm [100]. An interesting parenthetical fact can be added at this point. The high-temperature XRD pattern obtained at 100 °C was almost identical with the one at room temperature, but at 200 °C, the reflection was shifted to 11.2°. This narrowing of the interlayer space to 0.79 nm was linked to the removal of the water moieties between the layers of the wall. It is worth mentioning that thermogravimetric analysis of the NTBs showed that above 200 °C, the weight loss was very limited.

Going a step further, the team of Tanthapanichakoon [117] chose to study the effect of temperature during the synthesis with or without US pre-treatment by using raw particles of an ~ 400-nm diameter, due to the fact that this raw $TiO_2$ gave higher $S_{BET}$ compared to the raw one with average particle size of 1 μm. The resulted specific surface areas and the morphology of the sample are presented in Fig. 17.

As can be observed, the effect of US pretreatment on the structural and morphological features is loud and clear, and, additionally, it had a key effect on the product purity and shape homogeneity, as confirmed by microscopy analysis. At 90 °C, NTBs, nanosheets, and remaining un-transformed crystals were detected either without or with US pretreatment (Fig. 18). Moreover, the use of sonication did not lead to higher $S_{BET}$. The effect of US was dramatically more pronounced at a synthesis temperature of 120 °C. The length of the NTBs was much higher and the $S_{BET}$ almost doubled in value. The purity was also enhanced, since no un-transformed crystals were detected after US pre-treatment. Analogous outcomes were derived when the synthesis was performed at 150 °C after US pre-treatment. Further increase to 180 °C had a negative impact on the $S_{BET}$ and the desired morphology, with the US irradiation not leading to a specific effect. The predominant shape of the particles was of nanowires/fibers/rods in both cases, although with a smaller diameter in the case of US irradiation. The shape change was in good agreement with the angle shift of the XRD pattern, as was discussed above. It can be suggested that the thermal effects when the synthesis temperature is higher than 150 °C overcome the effects of the US pre-treatment.

## 3 PART B

### 3.1 Ball-Milling-Derived Nanomaterials

The utilization of ball milling (BM) in order to obtain $TiO_2$ nanoparticles includes different possible pathways with regard to the used raw material. The latter can be either elemental Ti, either $TiO_2$, or a different source of titanium like a mineral. The duration and the power of the BM plays a crucial role, as does the atmosphere in which the process takes place. The achievement of high temperature is found to be in some

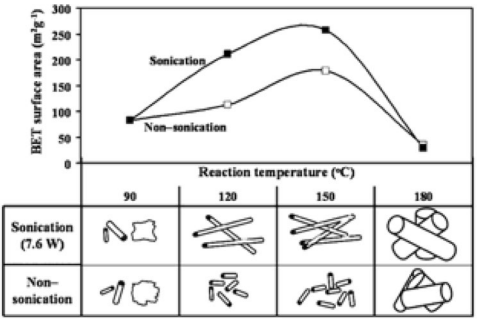


**Fig. 17** BET specific surface area and morphology/shape of titanate products synthesized (from raw $TiO_2$ of an avg. size of 400 nm) at reaction temperature of **a** 90 °C, **b** 120 °C, **c** 150 °C, and **d** 180 °C without or with US irradiation (power of 7.6 W). Reprinted with permission from [117]. Copyright (2009) Elsevier

cases a drawback, and for this reason, the ball milling is performed with breaks or even with the use of a liquid phase. The latter case is referred to as wet ball milling. In most reported cases and especially towards the formation of one dimensional $TiO_2$ nanostructures, ball milling was utilized as a mechanochemical pretreatment to obtain metastable polymorphs, that can be further tuned in morphology by annealing or wet chemistry. In this part, we collected some reports in which the application of ball milling dramatically affected the final properties of the nanomaterials. Starting with 0-D nanomaterials and ending with 1-D materials, we tried to introduce the reported results following a chronological order. An emphasis was given when the nanomaterials were found to possess an elevated photocatalytic capability.

### 3.2 0-D Ball-Milling-Derived Nanostructures

In 1994, Begin-Colin et al. studied the polymorphic transformation of $TiO_2$ from an anatase phase to a rutile phase by ball-milling (BM), based on XRD and Fourier transform infrared (FTIR ) spectroscopy techniques [119]. They observed that the phase transformation was not direct, since different transient phases appeared, with the one of type II being predominant. However, no electron microscopy analysis was performed. The importance of this study was the conclusion that the anatase-to-rutile transformation is not a direct process. Based on that, the authors emphasized that the ball-milling technique is feasible to obtain alloys with various non-equilibrium crystallographic phase materials. The intermediate crystallographic phases can further be tuned with various methods, in order to obtain desired photocatalytic properties.

An ultimately serious drawback of the ball-milling technique, especially when the target is a material of a high purity, is the possibility of atmospheric nitrogen incorporation into the structure or metal (predominately iron) from the used ball-milling apparatus. For instance, it was showed by Lu et al. [120] that, depending the atmosphere and the duration of the ball milling, different doping of N or Fe could result, even under air. More interesting, titanium oxynitrile instead of oxide can be obtained within a closed ball-milling system and extension of the mechanochemical process for up to 90 h. In 2007, Pang et al. [121] showed the possibility to synthesize a composite of titanium and hydroxyapatite by a wet ball-milling method. Hydroxyapatite (HP), $Ca_5(PO_4)_3(OH)$, is a natural mineral,

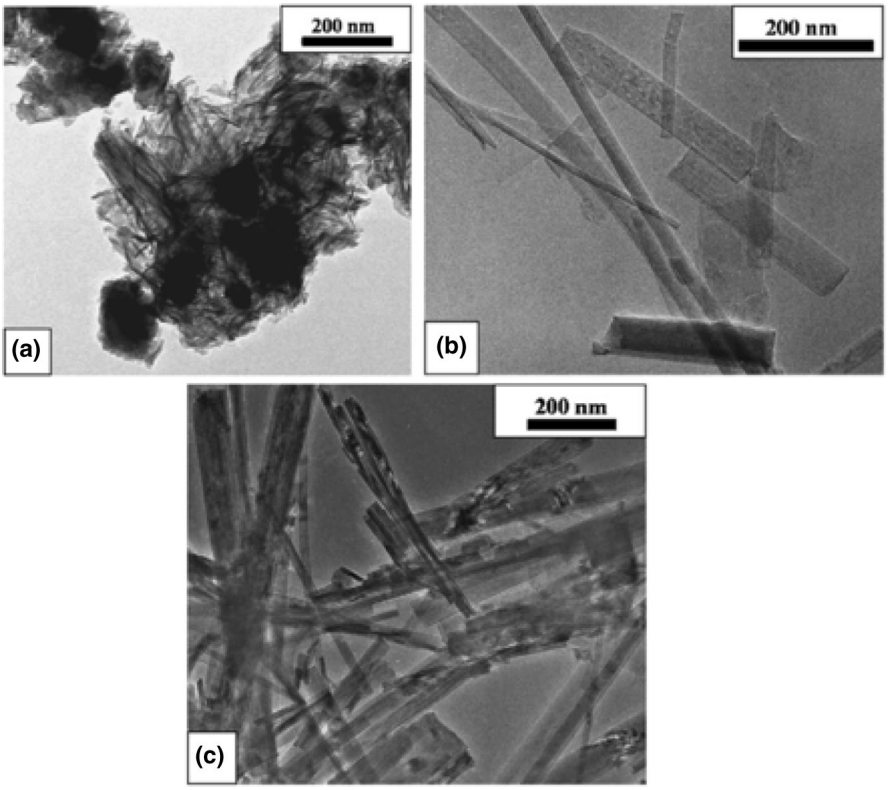


**Fig. 18** HRTEM captures of mixed titanate nanostructures obtained from raw $TiO_2$ (of an average particle size 400 nm) at reaction temperature of 90 °C (**a**) and titanate nanofibers/wires synthesized at 180 °C without sonication (**b**), and with power of 7.6 W (**c**). Adapted with permission from [117]. Copyright (2009) Elsevier

while modified forms of HP are the main compounds of human bones and teeth. The increase of milling duration led to the decrease of the grain size, as well as to an improvement on the homogenously distribution of nano-hydroxyapatite. Analogous composites were synthesized by ball milling the same year by Silva et al. starting with $Ca(H_2PO_4)_2$ and $TiO_2$ as the raw materials [122].

In 2000, Begin-Colin et al. studied in details the kinetics and mechanisms of phase transformations induced by ball milling in air, starting with a commercial anatase $TiO_2$ [123]. They concluded that the anatase is transformed by BM to rutile via a $TiO_2$ II phase. The powder-to-balls ratio of weights (R) influenced the transformation rate. Regarding the nature of ball-milling media, the transformation's kinetics were found faster in the case of alumina compared to steel.

Yadav et al. showed in 2015 the synthesis of titanium oxide nanoparticles from elemental powder of Ti (~0.5 mm) by ball milling for 10 h [124]. The size of the spherically shaped particles was between 10 and 20 nm, while XRD analysis indicated a pure rutile phase. The estimated bandgap was 4.46 eV. They used

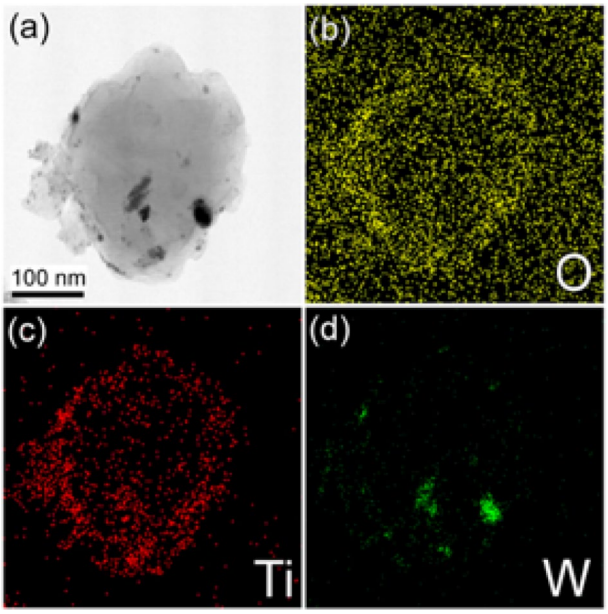


**Fig. 19** TEM image (**a**) and EDX maps (**b–d**) of $TiO_2$-coated boron particles wet-milled for 8 h. Reprinted with permission from [126]. Copyright (2016) MDPI

the obtained material in order to form a solid-state sensor by pelletization and application to an Ag–pellet–Ag electrode configuration. This sensor was found to possess a sensitivity toward liquefied petroleum gas (LPG). The author linked this to the blue-shift of the optical bandgap and to the nanoscaled morphology of the obtained ball-milling-derived nanoparticles.

In 2016, Rejender and Giri [125] presented an anomalous strain-evolution, crystallographic phase alteration, and bandgap narrowing by strain engineering using ball milling and commercially available $TiO_2$ powder as the precursor (particle size around 80 nm and bandgap 3.14 eV). Except for the decrement in size to 7–18 nm, the finally obtained $TiO_2$ nanocrystals (NCs) found to obtain a new crystallographic phase of $Ti_3O_5$, as well as a narrow bandgap of 2.71 eV.

Another interesting application of the wet ball-milling process was reported the same year by Jung et al. [126] for the $TiO_2$ nano-coating of boron particles. Briefly, a tungsten carbide milling jar was filled with titanium(IV) isopropoxide, boron powder (average particles' size ~ 800 nm), and hexane inside a glove box filled with nitrogen. The as-received suspension was further treated and washed with ethanol inside an US bath. They found that increase of the milling duration can lead to decrease of the final particle size, even up to ~ 150 nm. The particles were coated with an amorphous titania-containing layer (estimated 10 nm). The drawback of the extension of the ball milling was the incorporation of impurities, predominately tungsten, from the jar and balls, as can be seen in energy-dispersive X-ray (EDX) analysis (Fig. 19). The ball-milling-derived $TiO_2$-coated nanoparticles were promising for hydrogen and oxygen evolution reactions (HERs, OERs) in photoelectrochemical applications.

Another strategy to apply ball milling during the formation of $TiO_2$ nanoparticles was by mixing and ball milling of different precursors [36]. In 2007, Billik et al. used either $TiCl_4$ with $(NH_4)_2CO_3$ or $TiOSO_4{\cdot}xH_2O$ with $Na_2CO_3$ [127, 128]. After ball milling, they received amorphous samples, and they linked this to no crystallization having occurred. After annealing, they obtained well-crystalized materials, with higher photoreactivity compared to P25, determined by electron-paramagnetic-resonance (EPR) studies. They reported also that the presence of Fe impurities plays a role in the photoactivity of the final material. In 2008, Salari et al. also used $TiOSO_4{\cdot}xH_2O$ as the Ti source but NaCl as diluent [129].

### 3.3 1-D Ball-Milling-Derived Nanostructures

An important, abundant, and cheap source used for the industrial production of bulk $TiO_2$ is the iron–titanium oxide mineral ($FeTiO_3$) mineral, known as ilmenite. A high amount of ilmenite exists in the Earth's crust on all five continents, and on the Moon. The price of the raw material was around 80–107 USD per metric ton in 2004, while a peak was achieved in 2012 reaching even 350 USD per ton. In recent years, the cost has been around 250 USD/ton. The global demand has grown moderately in recent years, since it was estimated at around 6.4 million tons in 2010 with a prediction to reach above 8 million tons in 2025. The industrialized production of bulk $TiO_2$ from minerals is based on chloride or sulfate processes. In recent decades, there has been increased research effort to expand the use of this mineral in order to prepare nanostructures of $TiO_2$. The utilization of ball milling in order to promote the formation of nanostructured $TiO_2$ for a "real-life" application by using ball milling dates from 2008.

Li et al. (2008) [130] reported the formation of meso- and/or micro-porous hydrolysate $TiO_2$ by an initial mechanical activation of ilmenite using BM, following by a simultaneous dissolution and hydrolysis in a dilute sulfuric acid aqueous solution. The effect of the acid concentration played a key role in the structural parameters, with 10% sulfuric acid leading to a surface area of 258 $m^2/g$. In order to obtain the rutile-phased final material, calcination was applied. The importance of this work was that the ball-milling pretreatment made feasible the dissolution of the mineral in a dilute acidic solution. For an efficient decomposition in pigment production without mechanochemical utilization, an $H_2SO_4$ solution of a concentration above 80 wt% is required [130].

In 2011, Tao et al. prepared flower-like $FeTiO_3$ by pretreatment of ilmenite with high-energy BM followed by mild hydrothermal treatment in basic aqueous solution (1 M NaOH) [131]. They stated that the nano-petals comprising the final obtained flower-shaped particles had a thickness of 5–20 nm and sizes 100–200 nm. The hydrothermal treatment at 120 °C, even with 2 M NaOH, did not lead to noticeable changes in morphology. The obtained materials showed attractive capacitance values. Considering the above observations regarding the formation of NTBs, we can derive two possible conclusions/proposals. First, the presence of Fe stabilizes the layered structure of the nano-petals to roll to tubes. Second, the utilization of BM

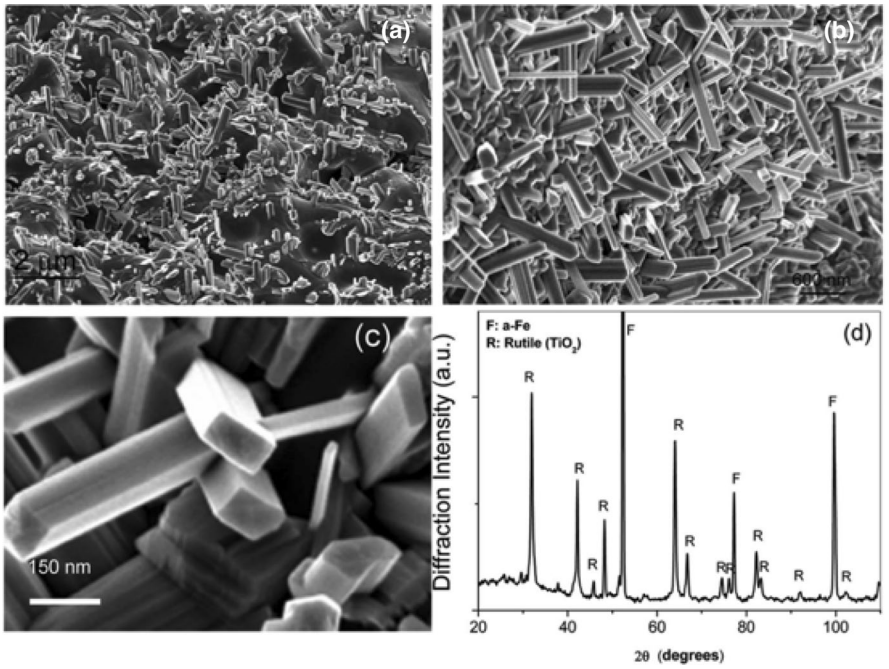


**Fig. 20** SEM image after the second annealing step at 700 °C for only 4 h (**a**), SEM image (**b**), a cross section of nanorods (**c**), and the XRD spectra (**d**) after annealing for 8 h at 700 °C. Adapted with permission from [133]. Copyright (2009) American Chemical Society

promotes the peeling of the mineral's particle even at a lower concentration of 10 M, necessary for the hydrothermal peeling of $TiO_2$ particles.

The formation of the 1-D nanorods obtained from ilmenite sand and the necessity of the metastable polymorphs formation was presented in 2008 and 2010 [132, 133]. It was revealed that for the formation of the nanorods, instead of other particle morphologies, the formation of the metastable phases like $Ti_2O_3$ to $Ti_3O_5$ is crucial. The ilmenite mineral was ball-milled with the presence of activated carbon at a ratio 4:1 at room temperature and under vacuum. The role of the latter as mechanical activation agent was to trigger the initial reduction to $TiO_2$. The obtained ultra-fine powder was annealed first at different high temperatures (900–1200 °C) in order to form the metastable phases. The low and controlled heating rate (5–10 °C) in an argon atmosphere with hydrogen flow was a critical step in order to obtain the desired metastable phases. It was reported that the presence of nitrogen led to an alternative redox reaction and iron nitride was formed. At temperature less than 1100 °C, the formed phase was rutile, which could remain in the same form after the second annealing step. The optimum duration of annealing was 8 h at 1200 °C, since prolonged heat treatment led to the formation of FeTi alloys. The second step of annealing was conducted at 700 °C in a $N_2$–5%$H_2$ atmosphere. The result was the gradual formation of $TiO_2$ nanorods and iron. As can be seen from the SEM images

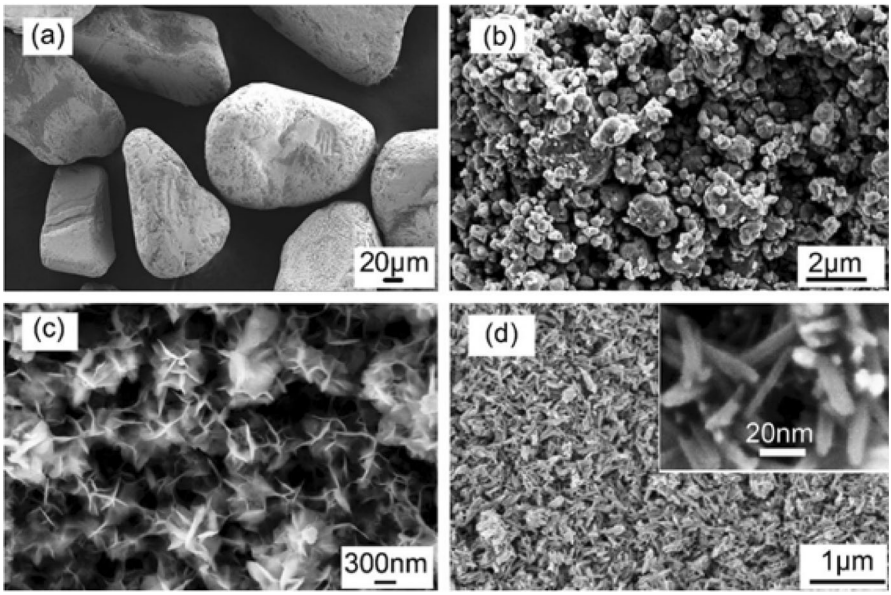


**Fig. 21** SEM images of original ilmenite powder (**a**), ball-milled ilmenite powder (**b**), flower-like $FeTiO_3$ nano-structures after treatment with NaOH (**c**), and the obtained nanorods after treatment with HCl for 8 h (**d**); inset: a higher-magnification capture of the nanorods. Reprinted with permission from [134]. Copyright (2013) Wiley

and XRD spectra in Fig. 20, the intermediate phase started to transform to nanorods after 4 h. The length of the nanorods was dependent on the time of annealing, and after 8 h, the intermediate phase was entirely transformed to rutile nanorods of the maximum length. Extension of the thermal treatment led to the sintering of the 1-D structure to coarse nanoparticles.

In 2013, Tao et al. [134] demonstrated a new method for the synthesis of $TiO_2$ nanorods (single-crystal) from natural ilmenite. The BM pre-treated mineral was further wet-chemistry-treated by mixing in a 2 M NaOH aqueous solution for 2 h at 120 °C, and flower-like $FeTiO_3$ nanoparticles were formed, but the authors concluded that this stage is an optional one. After short and mild drying, treatment with 4 M HCl at 90 °C for 4 h took place. The proposed mechanism was based on dissolution to $TiOCl_2$ and $FeCl_2$, hydrolysis, and precipitation. During the hydrolysis, $TiO_2$ crystals started to precipitate and grow in a 1-D fashion. The finally obtained rutile $TiO_2$ tetragonal nanorods (Fig. 21) had a length in the range of 50–100 nm, width of 5–20 nm, and thickness of 2–5 nm. The nanorods have also a moderately high specific area for this kind of nano-structure (up to 97 $m^2/g$). The most interesting outcome was that they showed excellent photocatalytic capability towards the photodegradation of oxalic acid, analogous with the one of Sigma–Aldrich's Degussa P25.

In 2014, Zhao et al. [135] reported the formation of spindle-like rutile $TiO_2$ nanorods from the dealloying in acidic conditions of an amorphous $Cu_{50}Ti_{50}$ alloy. The latter was formed by high-energy ball milling of elemental Cu and Ti in an

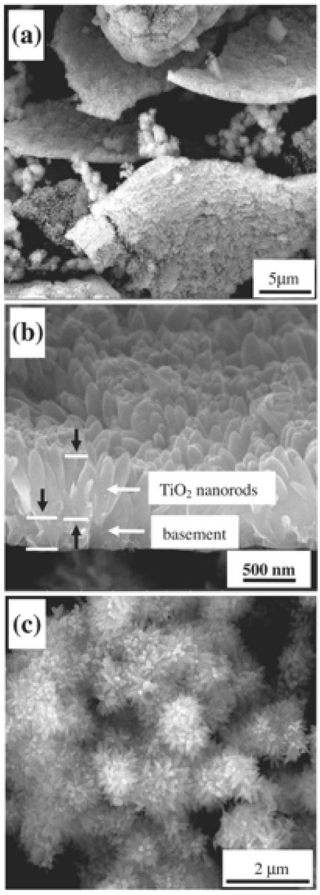


**Fig. 22** SEM images of ball-milling-derived amorphous $Cu_{50}Ti_{50}$ after immersing in $HNO_3$ aqueous solution for 48 h. Reprinted with permission from [135]. Copyright (2014) Elsevier

argon atmosphere. In order to avoid the high temperature as a result of the BM process, after milling for 0.5 h, there was an interruption for also 0.5 h. The as-received material was immersed in a highly concentrated $HNO_3$ aqueous solution (13.14 M) for dealloying. The obtained nanorods (Fig. 22) revealed a good photocatalytic degradation capability against the dye methyl orange under UV light irradiation, via the formation of radicals.

In the work of Zhao et al. [135], the involved steps/mechanism for the formation of the $TiO_2$ nanorods from the raw $Cu_{50}Ti_{50}$ alloy were proposed (Fig. 23). Titanium metal cannot react with nitric acid due to the presence of an oxide film. With the mechanical stress that is applied from the ball milling, the dealloying starts by corrosion from the outer surface and the removal of copper atoms and gradually continues to the inner part of the alloy.

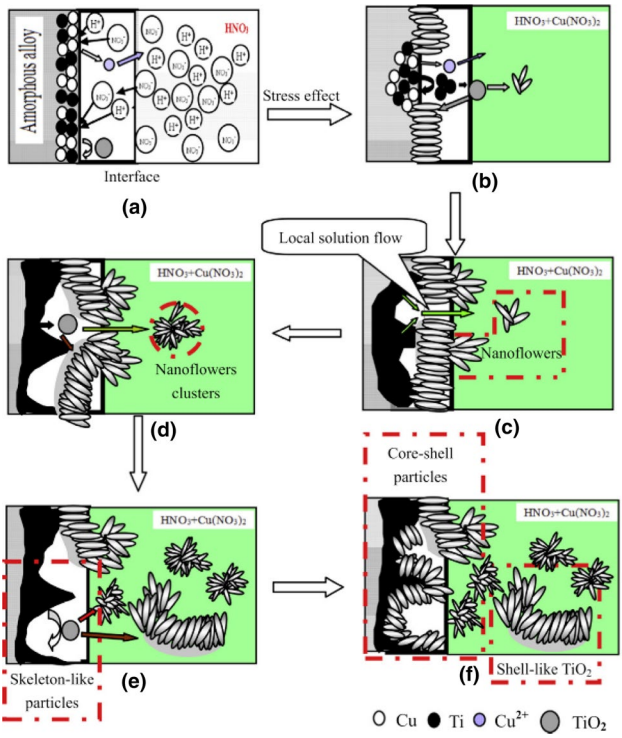


**Fig. 23** A schematic illustration of all the involved steps/mechanisms for the dealloying of amorphous $Cu_{50}Ti_{50}$ powders to rutile $TiO_2$ nanorods. Reprinted with permission from [135]. Copyright (2014) Elsevier

## 4 Conclusions—Prospectives

Taking into account all the above-mentioned results, it is reasonable to conclude that the formation of the hotspots as well the localized temperature increase during the mechanochemical treatment can antagonize the harsh conditions created inside the autoclave during the hydrothermal treatment, especially when the particle size of the precursor is equal or less than that of P25. It can be suggested that the thermal effects during the synthesis when the temperature is higher than 150 °C overcome the effects of the US pre-treatment. Especially in the case of a basic hydrothermal process, the utilization of sonication (US) as the pre-treatment has a vital role in the formation of 1-D nanostructures. The US effects can be further explored and applied for the synthesis of novel nano-engineered materials by other methods like precipitation, targeting towards the achievement of specific physical, chemical, and optical features.

In general, mechanochemistry can be a useful tool toward the manipulation of the important and desired features for different applications. Ball milling or US waves play a key role in size, shape, bandgap, porosity, light absorption, etc. Considering the above observations regarding the formation of NTBs, we can derive

two possible conclusions/proposals. First, the presence of Fe stabilizes the layered structure of the nano-petals to roll to tubes. Second, the utilization of BM promotes the peeling of the mineral's particle even at a lower concentration of 10 M, necessary for the hydrothermally peeling of $TiO_2$ particles.

The herein presented results showed that the mechanochemical-derived forces can promote the features of the catalyst, crucial for heterogeneous photocatalytic applications. While the main goal of the research effort towards the formation of 1-D $TiO_2$ up to nowadays was focused predominately on the explanation of the involved steps and mechanisms, in the cases where the materials were tested as photocatalyst, they revealed elevated photocatalytic capabilities, equal or better compared to the benchmark P25 in most of the cases. The goal of the present work is to highlight the developments in the area mechanochemical approaches when designing new synthetic strategies of nanostructured materials, as well as to call and initiate the attention for the possibilities for future utilization and exploration. We believe that nanoscaled and especially nanotubular-shaped titania can be further studied as photocatalyst, and we actively work towards this direction. Applying mechanochemistry will also be interesting to conduct for the design and synthesis of novel nanostructured electrodes for electrochemical catalytic reactions. Even though it is impossible these two techniques are simultaneously combined, the utilization of both at separate steps of synthesis can beget innovative approaches towards the synthesis of highly photo-active zero- and/or one-dimensional titanium-based catalyst, pure or doped with heteroatoms, like nitrogen or metals. In-depth study of the photocatalytic properties and applications of the $TiO_2$ NTBs, as, for instance, advanced oxidation processes or biomass valorization, can lead to interesting and important outcomes, as occurred in the case of their application in electrocatalysis and photo-remediation. Additionally, the use of a simple and economic US bath or ball-milling grinder can be utilized as a powerful synthetic tool. It is also important to point out that the use of mechanochemical processes in lab during the synthesis can lead to effects not yet studied, hypothesized, or imagined. Last but not least, we would like to emphasize that it will be absolutely beneficial if more details are provided when mechanochemistry is applied, such as calorimetric evaluation of the setup, luminol mapping, experimental setup details (horn details, photos, or a drawing), and details of the synthesis (yield, purity, size separation techniques, etc.).

**Acknowledgements** JCC and DAG are very grateful for the support from the National Science Centre in Poland within OPUS-13 project no. 2017/25/B/ST8/01592.

## References


1. Colmenares QJC (2013) Ultrasound and photochemical procedures for nanocatalysts preparation: application in photocatalytic biomass valorization. J Nanosci Nanotechnol 13:4787–4798. https://doi.org/10.1166/jnn.2013.7567
2. Chatel G, Valange S, Behling R, Colmenares JC (2017) A combined approach using sonochemistry and photocatalysis: how to apply sonophotocatalysis for biomass conversion? Chem Cat Chem 9:2615–2621. https://doi.org/10.1002/cctc.201700297
3. Rightmire NR, Hanusa TP (2016) Advances in organometallic synthesis with mechanochemical methods. Dalt Trans 45:2352–2362. https://doi.org/10.1039/c5dt03866a
4. Suslick KS (1995) Applications of ultrasound to materials chemistry. MRS Bull 20:29–34. https://doi.org/10.1557/S088376940004464X
5. Cerdan K, Ouyang W, Colmenares JC et al (2018) Facile mechanochemical modification of g-C3N 4 for selective photo-oxidation of benzyl alcohol. Chem Eng Sci. https://doi.org/10.1016/j.ces.2018.04.001
6. Colmenares JC, Lisowski P, Łomot D et al (2015) Sonophotodeposition of bimetallic photocatalysts Pd-Au/$TiO_2$: application to selective oxidation of methanol to methyl formate. Chemsuschem 8:1676–1685. https://doi.org/10.1002/cssc.201403125
7. James SL, Adams CJ, Bolm C et al (2012) Mechanochemistry: opportunities for new and cleaner synthesis. Chem Soc Rev 41:413–447. https://doi.org/10.1039/C1CS15171A
8. Magdziarz A, Colmenares JC, Chernyayeva O et al (2016) Iron-containing titania photocatalyst prepared by the sonophotodeposition method for the oxidation of benzyl alcohol. ChemCatChem 8:536–539. https://doi.org/10.1002/cctc.201501250
9. Kiss AA, Geertman R, Wierschem M et al (2018) Ultrasound-assisted emerging technologies for chemical processes. J Chem Technol Biotechnol 93:1219–1227. https://doi.org/10.1002/jctb.5555
10. Bhangu SK, Ashokkumar M (2017) Theory of sonochemistry. pp 1–28
11. Thornycroft JI (2009) Torpedo boat destroyers. J Am Soc Nav Eng 7:711–736. https://doi.org/10.1111/j.1559-3584.1895.tb04389.x
12. Neppiras EA (1980) Acoustic cavitation. Phys Rep 61:159–251. https://doi.org/10.1016/0370-1573(80)90115-5
13. Makino K, Mossoba MM, Riesz P (1982) Chemical effects of ultrasound on aqueous solutions. Evidence for hydroxyl and hydrogen free radicals (.cntdot. OH and .cntdot. H) by spin trapping. J Am Chem Soc 104:3537–3539. https://doi.org/10.1021/ja00376a064
14. Makino K, Mossoba MM, Riesz P (1983) Chemical effects of ultrasound on aqueous solutions. Formation of hydroxyl radicals and hydrogen atoms. J Phys Chem 87:1369–1377. https://doi.org/10.1021/j100231a020
15. Behling R, Chatel G, Valange S (2017) Sonochemical oxidation of vanillyl alcohol to vanillin in the presence of a cobalt oxide catalyst under mild conditions. Ultrason Sonochem 36:27–35. https://doi.org/10.1016/j.ultsonch.2016.11.015
16. Al-Juboori RA, Yusaf T, Bowtell L, Aravinthan V (2015) Energy characterisation of ultrasonic systems for industrial processes. Ultrasonics 57:18–30. https://doi.org/10.1016/j.ultras.2014.10.003
17. Toma M, Fukutomi S, Asakura Y, Koda S (2011) A calorimetric study of energy conversion efficiency of a sonochemical reactor at 500 kHz for organic solvents. Ultrason Sonochem 18:197–208. https://doi.org/10.1016/j.ultsonch.2010.05.005
18. Wood RJ, Lee J, Bussemaker MJ (2017) A parametric review of sonochemistry: control and augmentation of sonochemical activity in aqueous solutions. Ultrason Sonochem 38:351–370. https://doi.org/10.1016/j.ultsonch.2017.03.030
19. Suslick KS (1990) Sonochemistry. Science (80-) 247:1439–1445. https://doi.org/10.1126/science.247.4949.1439
20. Flint EB, Suslick KS (1991) The temperature of cavitation. Science 253:1397–1399. https://doi.org/10.1126/science.253.5026.1397
21. Suslick KS, Hammerton DA, Cline RE (1986) The sonochemical hot spot. J Am Chem Soc 108:5641–5642. https://doi.org/10.1021/ja00278a055
22. Pokhrel N, Vabbina PK, Pala N (2016) Sonochemistry: science and engineering. Ultrason Sonochem 29:104–128. https://doi.org/10.1016/j.ultsonch.2015.07.023
23. Cravotto G, Cintas P (2012) Harnessing mechanochemical effects with ultrasound-induced reactions. Chem Sci 3:295–307. https://doi.org/10.1039/c1sc00740h

24. Berlan J, Trabelsi F, Delmas H et al (1994) Oxidative degradation of phenol in aqueous media using ultrasound. Ultrason Sonochem 1:S97–S102. https://doi.org/10.1016/1350-4177(94)90005-1
25. Lepoint-Mullie F, De Pauw D, Lepoint T et al (1996) Nature of the "extreme conditions" in single sonoluminescing bubbles. J Phys Chem 100:12138–12141. https://doi.org/10.1021/jp9615060
26. Nikitenko SI, Pflieger R (2017) Toward a new paradigm for sonochemistry: short review on non-equilibrium plasma observations by means of MBSL spectroscopy in aqueous solutions. Ultrason Sonochem 35:623–630. https://doi.org/10.1016/j.ultsonch.2016.02.003
27. Margulis MA (1985) Sonoluminescence and sonochemical reactions in cavitation fields. A review. Ultrasonics 23:157–169. https://doi.org/10.1016/0041-624X(85)90024-1
28. Hua I, Hoechemer RH, Hoffmann MR (1995) Sonolytic hydrolysis of p-nitrophenyl acetate: the role of supercritical water. J Phys Chem 99:2335–2342. https://doi.org/10.1021/j100008a015
29. Yasuda K, Torii T, Yasui K et al (2007) Enhancement of sonochemical reaction of terephthalate ion by superposition of ultrasonic fields of various frequencies. Ultrason Sonochem 14:699–704. https://doi.org/10.1016/j.ultsonch.2006.12.013
30. Son Y (2017) Simple design strategy for bath-type high-frequency sonoreactors. Chem Eng J 328:654–664. https://doi.org/10.1016/j.cej.2017.07.012
31. Kojima Y, Asakura Y, Sugiyama G, Koda S (2010) The effects of acoustic flow and mechanical flow on the sonochemical efficiency in a rectangular sonochemical reactor. Ultrason Sonochem 17:978–984. https://doi.org/10.1016/j.ultsonch.2009.11.020
32. Guo J, Zhu S, Chen Z et al (2011) Sonochemical synthesis of $TiO_2$ nanoparticles on graphene for use as photocatalyst. Ultrason Sonochem 18:1082–1090. https://doi.org/10.1016/j.ultsonch.2011.03.021
33. Ouyang W, Kuna E, Yepez A et al (2016) Mechanochemical synthesis of $TiO_2$ nanocomposites as photocatalysts for benzyl alcohol photo-oxidation. Nanomaterials 6:93. https://doi.org/10.3390/nano6050093
34. Chatel G (2018) How sonochemistry contributes to green chemistry? Ultrason Sonochem 40:117–122. https://doi.org/10.1016/j.ultsonch.2017.03.029
35. Takacs L (2013) The historical development of mechanochemistry. Chem Soc Rev 42:7649–7659. https://doi.org/10.1039/c2cs35442j
36. Balaz P (2008) Mechanochemistry in nanoscience and minerals engineering. Springer, Berlin
37. Kipp S, Šepelák V, Becker KD (2005) Mechanochemie: chemie mit dem hammer. Chemie Unserer Zeit 39:384–392. https://doi.org/10.1002/ciuz.200500355
38. Stodart J, Faraday M (1820) V. Experiments on the alloys of steel, made with a view to its improvement. Philos Mag 56:26–35. https://doi.org/10.1080/14786442008652361
39. Takacs L (2003) M.Carey Lea, the father of mechanochemistry. Bull Hist Chem 28:26–34
40. Šepelák V, Düvel A, Wilkening M et al (2013) Mechanochemical reactions and syntheses of oxides. Chem Soc Rev 42:7507–7520. https://doi.org/10.1039/c2cs35462d
41. Takacs L (2018) Two important periods in the history of mechanochemistry. J Mater Sci 53:13324–13330. https://doi.org/10.1007/s10853-018-2198-3
42. Ostwald W (1919) Die chemische literatur und die organisation der wissenschaft. Akad Verlag, Gesel
43. Boldyreva E (2013) Mechanochemistry of inorganic and organic systems: what is similar, what is different? Chem Soc Rev 42:7719–7738. https://doi.org/10.1039/c3cs60052a
44. Takacs L (2014) What is unique about mechanochemical reactions? Acta Phys Pol A 126:1040–1043. https://doi.org/10.12693/APhysPolA.126.1040
45. Fujishima A, Honda K (1972) Electrochemical photolysis of water at a semiconductor electrode. Nature 238:37–38. https://doi.org/10.1038/238037a0
46. Colmenares JC, Luque R, Campelo JM et al (2009) Nanostructured photocatalysts and their applications in the photocatalytic transformation of lignocellulosic biomass: an overview. Materials (Basel) 2:2228–2258. https://doi.org/10.3390/ma2042228
47. Colmenares JC, Luque R (2014) Heterogeneous photocatalytic nanomaterials: prospects and challenges in selective transformations of biomass-derived compounds. Chem Soc Rev 43:765–778. https://doi.org/10.1039/C3CS60262A
48. Ibhadon A, Fitzpatrick P (2013) Heterogeneous photocatalysis: recent advances and applications. Catalysts 3:189–218. https://doi.org/10.3390/catal3010189
49. Aravindan V, Lee Y-S, Yazami R, Madhavi S (2015) $TiO_2$ polymorphs in 'rocking-chair' Li-ion batteries. Mater Today 18:345–351. https://doi.org/10.1016/j.mattod.2015.02.015

50. Vuyyuru KR, Strasser P (2012) Oxidation of biomass derived 5-hydroxymethylfurfural using heterogeneous and electrochemical catalysis. Catal Today 195:144–154. https://doi.org/10.1016/j.cattod.2012.05.008
51. Li SH, Liu S, Colmenares JC, Xu YJ (2016) A sustainable approach for lignin valorization by heterogeneous photocatalysis. Green Chem 18:594–607. https://doi.org/10.1039/c5gc02109j
52. Huang W, Tang X, Wang Y et al (2000) Selective synthesis of anatase and rutile via ultrasound irradiation. Chem Commun. https://doi.org/10.1039/b003349i
53. Palmisano G, Yurdakal S, Augugliaro V et al (2007) Photocatalytic selective oxidation of 4-methoxybenzyl alcohol to aldehyde in aqueous suspension of home-prepared titanium dioxide catalyst. Adv Synth Catal 349:964–970. https://doi.org/10.1002/adsc.200600435
54. Chen X, Mao SS (2007) Titanium dioxide nanomaterials: synthesis, properties, modifications and applications. Chem Rev 107:2891–2959. https://doi.org/10.1021/cr0500535
55. Gupta SM, Tripathi M (2011) A review of $TiO_2$ nanoparticles. Chin Sci Bull 56:1639–1657. https://doi.org/10.1007/s11434-011-4476-1
56. Zatloukalová K, Obalová L, Kočí K et al (2017) Photocatalytic degradation of endocrine disruptor compounds in water over immobilized $TiO_2$ photocatalysts. Iran J Chem Chem Eng 2017:36
57. Higashimoto S, Kitao N, Yoshida N et al (2009) Selective photocatalytic oxidation of benzyl alcohol and its derivatives into corresponding aldehydes by molecular oxygen on titanium dioxide under visible light irradiation. J Catal 266:279–285. https://doi.org/10.1016/j.jcat.2009.06.018
58. Giannakoudakis DA, Arcibar-Orozco JA, Bandosz TJ (2015) Key role of terminal hydroxyl groups and visible light in the reactive adsorption/catalytic conversion of mustard gas surrogate on zinc (hydr)oxides. Appl Catal B Environ 174:96–104. https://doi.org/10.1016/j.apcatb.2015.02.028
59. Li D, Haneda H (2003) Morphologies of zinc oxide particles and their effects on photocatalysis. Chemosphere 51:129–137. https://doi.org/10.1016/S0045-6535(02)00787-7
60. Szabó T, Németh J, Dékány I (2003) Zinc oxide nanoparticles incorporated in ultrathin layer silicate films and their photocatalytic properties. Colloids Surfaces A Physicochem Eng Asp 230:23–35. https://doi.org/10.1016/j.colsurfa.2003.09.010
61. Giannakoudakis DA, Nair V, Khan A et al (2019) Additive-free photo-assisted selective partial oxidation at ambient conditions of 5-hydroxymethylfurfural by manganese (IV) oxide nanorods. Appl Catal B Environ 256:117803. https://doi.org/10.1016/j.apcatb.2019.117803
62. Jun YS, Hong WH, Antonietti M, Thomas A (2009) Mesoporous, 2D hexagonal carbon nitride and titanium nitride/carbon composites. Adv Mater 21:4270–4274. https://doi.org/10.1002/adma.200803500
63. Chen X, Jun Y-S, Takanabe K et al (2009) Ordered mesoporous SBA-15 type graphitic carbon nitride: a semiconductor host structure for photocatalytic hydrogen evolution with visible light. Chem Mater 21:4093–4095. https://doi.org/10.1021/cm902130z
64. Giannakoudakis DA, Seredych M, Rodríguez-Castellón E, Bandosz TJ (2016) Mesoporous graphitic carbon nitride-based nanospheres as visible-light active chemical warfare agents decontaminant. ChemNanoMat 2:268–272. https://doi.org/10.1002/cnma.201600030
65. Wei H, Zhang Q, Zhang Y et al (2016) Enhancement of the Cr(VI) adsorption and photocatalytic reduction activity of g-$C_3N_4$ by hydrothermal treatment in $HNO_3$ aqueous solution. Appl Catal A Gen 521:9–18. https://doi.org/10.1016/j.apcata.2015.11.005
66. Antonakou EV, Kalogiannis KG, Stefanidis SD et al (2014) Catalytic and thermal pyrolysis of polycarbonate in a fixed-bed reactor: the effect of catalysts on products yields and composition. Polym Degrad Stab 110:482–491. https://doi.org/10.1016/j.polymdegradstab.2014.10.007
67. Saroyan HS, Bele S, Giannakoudakis DA et al (2019) Degradation of endocrine disruptor, bisphenol-A, on an mixed oxidation state manganese oxide/modified graphite oxide composite: a role of carbonaceous phase. J Colloid Interface Sci 539:516–524. https://doi.org/10.1016/j.jcis.2018.12.088
68. Stefanidis SD, Karakoulia SA, Kalogiannis KG et al (2016) Natural magnesium oxide (MgO) catalysts: a cost-effective sustainable alternative to acid zeolites for the in situ upgrading of biomass fast pyrolysis oil. Appl Catal B Environ 196:155–173. https://doi.org/10.1016/j.apcatb.2016.05.031
69. Han C, Tang ZR, Liu J et al (2019) Efficient photoredox conversion of alcohol to aldehyde and $H_2$ by heterointerface engineering of bimetal-semiconductor hybrids. Chem Sci 10:3514–3522. https://doi.org/10.1039/c8sc05813j
70. Giannakoudakis DADA, Hu Y, Florent M, Bandosz TJTJTJ (2017) Smart textiles of MOF/g-C 3N 4 nanospheres for the rapid detection/detoxification of chemical warfare agents. Nanosc Horiz 2:356–364. https://doi.org/10.1039/C7NH00081B

71. Giannakoudakis DA, Bandosz TJ (2018) Detoxification of chemical warfare agents, 1st edn. Springer, Cham
72. Lombardi J, Yang L, Pearsall FA et al (2019) Stoichiometric control over ferroic behavior in Ba(Ti 1–x Fe x)$O_3$ nanocrystals. Chem Mater 31:1318–1335. https://doi.org/10.1021/acs.chemmater.8b04447
73. Weng B, Liu S, Tang ZR, Xu YJ (2014) One-dimensional nanostructure based materials for versatile photocatalytic applications. RSC Adv 4:12685–12700. https://doi.org/10.1039/c3ra47910b
74. Li JY, Yuan L, Li SH et al (2019) One-dimensional copper-based heterostructures toward photo-driven reduction of $CO_2$ to sustainable fuels and feedstocks. J Mater Chem A 7:8676–8689. https://doi.org/10.1039/c8ta12427b
75. Tang ZR, Han B, Han C, Xu YJ (2017) One dimensional CdS based materials for artificial photoredox reactions. J Mater Chem A 5:2387–2410. https://doi.org/10.1039/C6TA06373J
76. Liu S, Yang MQ, Tang ZR, Xu YJ (2014) A nanotree-like CdS/ZnO nanocomposite with spatially branched hierarchical structure for photocatalytic fine-chemical synthesis. Nanoscale 6:7193–7198. https://doi.org/10.1039/c4nr01227e
77. Liu S, Tang ZR, Sun Y et al (2015) One-dimension-based spatially ordered architectures for solar energy conversion. Chem Soc Rev 44:5053–5075. https://doi.org/10.1039/c4cs00408f
78. Giannakoudakis DA, Florent M, Wallace R et al (2018) Zinc peroxide nanoparticles: surface, chemical and optical properties and the effect of thermal treatment on the detoxification of mustard gas. Appl Catal B Environ 226:429–440. https://doi.org/10.1016/j.apcatb.2017.12.068
79. Magdziarz A, Colmenares JC, Chernyayeva O et al (2017) Insight into the synthesis procedure of $Fe_3$+/$TiO_2$-based photocatalyst applied in the selective photo-oxidation of benzyl alcohol under sun-imitating lamp. Ultrason Sonochem 38:187–196. https://doi.org/10.1016/j.ultsonch.2017.03.012
80. Giannakoudakis DA, Pearsall F, Florent M et al (2018) Barium titanate perovskite nanoparticles as a photoreactive medium for chemical warfare agent detoxification. J Colloid Interface Sci 531:233–244. https://doi.org/10.1016/j.jcis.2018.07.053
81. Hoyer P (1996) Formation of a titanium dioxide nanotube array. Langmuir 12:1411–1413. https://doi.org/10.1021/la9507803
82. Antonelli DM, Ying JY (1995) Synthesis of hexagonally packed mesoporous $TiO_2$ by a modified sol–gel method. Angew Chemie Int Ed English 34:2014–2017. https://doi.org/10.1002/anie.199520141
83. Wang Y, Tang X, Yin L et al (2000) Sonochemical synthesis of mesoporous titanium oxide with wormhole-like framework structures. Adv Mater 12:1183–1186. https://doi.org/10.1002/1521-4095(200008)12:16%3c1183:AID-ADMA1183%3e3.0.CO;2-X
84. Antonelli DM (1999) Synthesis of phosphorus-free mesoporous titania via templating with amine surfactants. Micropor Mesopor Mater 30:315–319. https://doi.org/10.1016/S1387-1811(99)00042-6
85. Yu JC, Yu J, Ho W, Zhang L (2001) Preparation of highly photocatalytic active nano-sized $TiO_2$ particles via ultrasonic irradiation. Chem Commun 2001:1942–1943. https://doi.org/10.1039/b105471f
86. Ghows N, Entezari MH (2010) Ultrasound with low intensity assisted the synthesis of nanocrystalline $TiO_2$ without calcination. Ultrason Sonochem 17:878–883. https://doi.org/10.1016/j.ultsonch.2010.03.010
87. Chen X, Liu L, Yu PY, Mao SS (2011) Increasing solar absorption for photocatalysis with black hydrogenated titanium dioxide nanocrystals. Science (80–) 331:746–750. https://doi.org/10.1126/science.1200448
88. Osorio-Vargas PA, Pulgarin C, Sienkiewicz A et al (2012) Low-frequency ultrasound induces oxygen vacancies formation and visible light absorption in $TiO_2$ P-25 nanoparticles. Ultrason Sonochem 19:383–386. https://doi.org/10.1016/j.ultsonch.2011.11.013
89. Fan C, Chen C, Wang J et al (2015) Black hydroxylated titanium dioxide prepared via ultrasonication with enhanced photocatalytic activity. Sci Rep 5:11712. https://doi.org/10.1038/srep11712
90. Fan C, Chen C, Wang J et al (2014) Enhanced photocatalytic activity of hydroxylated and N-doped anatase derived from amorphous hydrate. J Mater Chem A 2:16242–16249. https://doi.org/10.1039/c4ta03179b
91. Thommes M, Kaneko K, Neimark AV et al (2015) Physisorption of gases, with special reference to the evaluation of surface area and pore size distribution (IUPAC Technical Report). Pure Appl Chem 87:1051–1069. https://doi.org/10.1515/pac-2014-1117

92. Li W, Liu M, Feng S et al (2014) Template-free synthesis of uniform magnetic mesoporous $TiO_2$ nanospindles for highly selective enrichment of phosphopeptides. Mater Horizons 1:439–445. https://doi.org/10.1039/c4mh00030g
93. Comini E, Baratto C, Faglia G et al (2009) Quasi-one dimensional metal oxide semiconductors: preparation, characterization and application as chemical sensors. Prog Mater Sci 54:1–67. https://doi.org/10.1016/j.pmatsci.2008.06.003
94. Roy P, Berger S, Schmuki P (2011) $TiO_2$ nanotubes: synthesis and applications. Angew Chemie Int Ed 50:2904–2939. https://doi.org/10.1002/anie.201001374
95. Kasuga T, Hiramatsu M, Hoson A et al (1998) Formation of titanium oxide nanotube. Langmuir 14:3160–3163. https://doi.org/10.1021/la9713816
96. Du GH, Chen Q, Che RC et al (2001) Preparation and structure analysis of titanium oxide nanotubes. Appl Phys Lett 79:3702–3704. https://doi.org/10.1063/1.1423403
97. Chen Q, Zhou W, Du GH, Peng LM (2002) Trititanate nanotubes made via a single alkali treatment. Adv Mater 14:2000–2003. https://doi.org/10.1002/1521-4095(20020903)14:17%3c1208:AID-ADMA1208%3e3.0.CO;2-0
98. Zhang S, Peng L-M, Chen Q et al (2003) Formation mechanism of $H_2Ti_3O_7$ nanotubes. Phys Rev Lett 91:2–5. https://doi.org/10.1103/physrevlett.91.256103
99. Chen Q, Du GH, Zhang S, Peng L-M (2002) The structure of trititanate nanotubes. Acta Crystallogr Sect B Struct Sci 58:587–593. https://doi.org/10.1107/S0108768102009084
100. Suzuki Y, Yoshikawa S (2004) Synthesis and thermal analyses of $TiO_2$-derived nanotubes prepared by the hydrothermal method. J Mater Res 19:982–985. https://doi.org/10.1557/JMR.2004.0128
101. Kasuga T, Hiramatsu M, Hoson A et al (1999) Titania nanotubes prepared by chemical processing. Adv Mater 11:1307–1311. https://doi.org/10.1002/(SICI)1521-4095(199910)11:15%3c1307:AID-ADMA1307%3e3.0.CO;2-H
102. Nakahira A, Kubo T, Numako C (2010) Formation mechanism of $TiO_2$-derived titanate nanotubes prepared by the hydrothermal process. Inorg Chem 49:5845–5852. https://doi.org/10.1021/ic9025816
103. Bavykin DV, Parmon VN, Lapkin AA, Walsh FC (2004) The effect of hydrothermal conditions on the mesoporous structure of $TiO_2$ nanotubes. J Mater Chem 14:3370–3377. https://doi.org/10.1039/b406378c
104. Seo DS, Lee JK, Kim H (2001) Preparation of nanotube-shaped $TiO_2$ powder. J Cryst Growth 229:428–432. https://doi.org/10.1016/S0022-0248(01)01196-4
105. Zhang Q, Gao L, Sun J, Zheng S (2002) Preparation of long $TiO_2$ nanotubes from ultrafine rutile nanocrystals. Chem Lett 31:226–227. https://doi.org/10.1246/cl.2002.226
106. Bai Q, Lavenas M, Vauriot L et al (2019) Hydrothermal transformation of titanate scrolled nanosheets to anatase over a wide pH range and contribution of triethanolamine and oleic acid to control the morphology. Inorg Chem 58:2588–2598. https://doi.org/10.1021/acs.inorgchem.8b03197
107. Bin Liu, Eray S, Aydil (2009) Growth of oriented single-crystalline rutile $TiO_2$ nanorods on transparent conducting substrates for dye-sensitized solar cells. J Am Chem Soc 113:3985–3990
108. Pavasupree S, Suzuki Y, Yoshikawa S, Kawahata R (2005) Synthesis of titanate, $TiO_2$ (B), and anatase $TiO_2$ nanofibers from natural rutile sand. J Solid State Chem 178:3110–3116. https://doi.org/10.1016/j.jssc.2005.07.022
109. Tsai CC, Teng H (2004) Regulation of the physical characteristics of titania nanotube aggregates synthesized from hydrothermal treatment. Chem Mater 16:4352–4358. https://doi.org/10.1021/cm049643u
110. Oskam G, Nellore A, Penn RL, Searson PC (2003) The growth kinetics of $TiO_2$ nanoparticles from titanium(IV) alkoxide at high water/titanium ratio. J Phys Chem B 107:1734–1738. https://doi.org/10.1021/jp021237f
111. Wong CL, Tan YN, Mohamed AR (2011) A review on the formation of titania nanotube photocatalysts by hydrothermal treatment. J Environ Manage 92:1669–1680. https://doi.org/10.1016/j.jenvman.2011.03.006
112. Zhu Y, Li H, Koltypin Y et al (2001) Sonochemical synthesis of titania whiskers and nanotubes. Chem Commun 24:2616–2617. https://doi.org/10.1039/b108968b
113. Izawa H, Kikkawa S, Koizumi M (1982) Ion exchange and dehydration of layered [sodium and potassium] titanates, $Na_2Ti_3O_7$ and $K_2Ti_4O_9$. J Phys Chem 86:5023–5026. https://doi.org/10.1021/j100222a036

114. Marchand R, Brohan L, Tournoux M (1980) $TiO_2$(B) a new form of titanium dioxide and the potassium octatitanate $K_2Ti_8O_{17}$. Mater Res Bull 15:1129–1133. https://doi.org/10.1016/0025-5408(80)90076-8
115. Joo J, Kwon SG, Yu T et al (2005) Large-scale synthesis of $TiO_2$ nanorods via nonhydrolytic sol–gel ester elimination reaction and their application to photocatalytic inactivation of *E. coli*. J Phys Chem B 109:15297–15302. https://doi.org/10.1021/jp052458z
116. Ma Y, Lin Y, Xiao X et al (2006) Sonication–hydrothermal combination technique for the synthesis of titanate nanotubes from commercially available precursors. Mater Res Bull 41:237–243. https://doi.org/10.1016/j.materresbull.2005.08.020
117. Viriya-empikul N, Charinpanitkul T, Sano N et al (2009) Effect of preparation variables on morphology and anatase-brookite phase transition in sonication assisted hydrothermal reaction for synthesis of titanate nanostructures. Mater Chem Phys 118:254–258. https://doi.org/10.1016/j.matchemphys.2009.07.042
118. Viriya-Empikul N, Sano N, Charinpanitkul T et al (2008) A step towards length control of titanate nanotubes using hydrothermal reaction with sonication pretreatment. Nanotechnology. https://doi.org/10.1088/0957-4484/19/03/035601
119. Begin-Colin S, Le Caer G, Mocellin A, Zandona M (1994) Polymorphie transformations of titania induced by ball milling. Philos Mag Lett 69:1–7. https://doi.org/10.1080/09500839408242430
120. Lu CJ, Zhang J, Li ZQ (2004) Structural evolution of titanium powder during ball milling in different atmospheres. J Alloys Compd 381:278–283. https://doi.org/10.1016/j.jallcom.2004.03.130
121. Pang P, Li W, Liu Y (2007) Effect of ball milling process on the microstructure of titanium-nanohydroxyapatite composite powder. Rare Met 26:118–123. https://doi.org/10.1016/S1001-0521(07)60170-3
122. Silva CC, Graça MPF, Valente MA, Sombra ASB (2007) Crystallite size study of nanocrystalline hydroxyapatite and ceramic system with titanium oxide obtained by dry ball milling. J Mater Sci 42:3851–3855. https://doi.org/10.1007/s10853-006-0474-0
123. Bégin-Colin S, Girot T, Le Caër G, Mocellin A (2000) Kinetics and mechanisms of phase transformations induced by ball-milling in anatase $TiO_2$. J Solid State Chem 149:41–48. https://doi.org/10.1006/jssc.1999.8491
124. Yadav BC, Singh S, Yadav TP (2015) Titania prepared by ball milling: its characterization and application as liquefied petroleum gas sensor. Synth React Inorg Met Nano-Metal Chem 45:487–494. https://doi.org/10.1080/15533174.2012.749892
125. Rajender G, Giri PK (2016) Strain induced phase formation, microstructural evolution and band-gap narrowing in strained $TiO_2$ nanocrystals grown by ball milling. J Alloys Compd 676:591–600. https://doi.org/10.1016/j.jallcom.2016.03.154
126. Jung HJ, Nam K, Sung HG et al (2016) Preparation of $TiO_2$-decorated boron particles by wet ball milling and their photoelectrochemical hydrogen and oxygen evolution reactions. Materials (Basel). https://doi.org/10.3390/ma9121012
127. Billik P, Plesch G (2007) Mechanochemical synthesis of nanocrystalline $TiO_2$ from liquid TiCl4. Scr Mater 56:979–982. https://doi.org/10.1016/j.scriptamat.2007.01.048
128. Billik P, Plesch G, Brezová V et al (2007) Anatase $TiO_2$ nanocrystals prepared by mechanochemical synthesis and their photochemical activity studied by EPR spectroscopy. J Phys Chem Solids 68:1112–1116. https://doi.org/10.1016/j.jpcs.2007.02.010
129. Salari M, Rezaee M, Marashi SPH, Aboutalebi SH (2009) The role of the diluent phase in the mechanochemical preparation of $TiO_2$ nanoparticles. Powder Technol 192:54–57. https://doi.org/10.1016/j.powtec.2008.11.011
130. Li C, Liang B, Song H et al (2008) Preparation of porous rutile titania from ilmenite by mechanical activation and subsequent sulfuric acid leaching. Microporous Mesoporous Mater 115:293–300. https://doi.org/10.1016/j.micromeso.2008.01.045
131. Tao T, Glushenkov AM, Liu H et al (2011) Ilmenite $FeTiO_3$ nanoflowers and their pseudocapacitance. J Phys Chem C 115:17297–17302. https://doi.org/10.1021/jp203345s
132. Yu J, Chen Y (2010) One-dimensional growth of $TiO_2$ nanorods from ilmenite sands. J Alloys Compd 504:S364–S367. https://doi.org/10.1016/j.jallcom.2010.02.145
133. Yu J, Chen Y, Glushenkov AM (2009) Titanium oxide nanorods extracted from ilmenite sands. Cryst Growth Des 9:1240–1244. https://doi.org/10.1021/cg801125w
134. Tao T, Chen Y, Zhou D et al (2013) Expanding the applications of the ilmenite mineral to the preparation of nanostructures: $TiO_2$ nanorods and their photocatalytic properties in the degradation of oxalic acid. Chem A Eur J 19:1091–1096. https://doi.org/10.1002/chem.201202451

135. Zhao Z, Xu J, Liaw PK et al (2014) One-step formation and photocatalytic performance of spindle-like $TiO_2$ nanorods synthesized by dealloying amorphous $Cu_{50}Ti_{50}$ alloy. Corros Sci 84:66–73. https://doi.org/10.1016/j.corsci.2014.03.014